High northern geomagnetic field behavior and new constraints on the Gilsá event: Paleomagnetic and $^{40}Ar/^{39}Ar$ results of ∼0.5–3.1 Ma basalts from Jökuldalur, Iceland.

Arne Døssing[a,b,*], Adrian R. Muxworthy[b], Radchagrit Supakulopas[b], Morten S. Riishuus[c], Conall Mac Niocaill[d]

[a] *Div. of Geomagnetism, DTU Space, Technical University of Denmark, Diplomvej, Building 371, 2800 Kgs. Lyngby, Denmark*
[b] *Dept. of Earth Science and Engineering, Imperial College London, South Kensington Campus, London SW7 2AZ, UK*
[c] *Nordic Volcanological Center, Institute of Earth Sciences, University of Iceland, Sturlugata 7, IS-101 Reykjavik*
[d] *Dept. of Earth Sciences, University of Oxford, S Parks Rd, Oxford OX1 3AN, UK*

Abstract

Recent paleomagnetic results of extrusive rocks from high southern latitudes ($> 60°$S) and high northern latitudes ($> 60°$N) have been suggested to reflect a hemispheric asymmetry of the geomagnetic field on time-scales of 10^5 to 10^6 years, with higher and more stable fields in the north. This interpretation, however, is based on only a few modern-standard paleodirectional data sets and on high northern stable field paleointensity data of rocks that are mainly younger than 100 kyr. The sparsity of modern-standard data questions the validity (and age range) of this potential geomagnetic asymmetry. In 2013 and 2014, we sampled basaltic lava flows in Jökuldalur, north-eastern Iceland, to obtain high-standard paleodirectional and paleointensity data at relatively

*Corresponding author
Email address: ards@space.dtu.dk (Arne Døssing)

high-northern latitudes (65.2°N). On average, we sampled >15 cores per site at 51 sites of predominantly Matuyama age. Complete demagnetization was carried out on all samples using AF or thermal demagnetization. We present 45 distinct paleomagnetic directions based on overall $N > 10$ ChRMs per site and $\alpha 95 < 3.5°$. We obtain a mean direction of D =355.7°, I =76.3°, and $\alpha 95$ =3.2 for N =45 sites that is not significantly different from a GAD field. The resulting 45 VGPs distribute around the North Pole, and the global mean paleomagnetic pole ($\bar{\lambda} = 87.8°$, $\bar{\phi} = 224.3°$) is coincident with the North Pole within the $\alpha 95$ confidence limit. We calculate a VGP dispersion for our 38 Matuyama age sites of $20.5^{\frac{23.3}{17.8}}$, which is ∼1–4° lower than estimates from published Iceland data (from surveys that sampled 2–5 cores per site) but still supports the interpretation of a dependence of VGP dispersion on latitude during the Matuyama. Based on relatively strict cut-off criteria we also present six new field strength estimates from the time interval ∼1.2–1.83 Ma, thus filling a large data gap of the high-northern stable field behaviour. We obtain a median VADM of 57±3 ZAm^2 (VDM of 60±5 Am^2), which is higher than the median VADM of 16 intensity estimates from Antarctica (39±7 ZAm^2) from the same period. A higher northern field is also found when using less strict cut-off criteria resulting in 14 field estimates from Jökuldalur, i.e. we find support for higher field strength in the northern hemisphere as compared to the southern hemisphere during the Matuyama. Finally, we deliver a revised magneto-chronostratigraphic model of Jökuldalur and conduct an investigation of the type sections of the so-called Gilsá normal polarity event around 1.62 Ma. Our revised model is based on 11 new ^{40}Ar/^{39}Ar ages. No evidence is found of the existence of the

Gilsá event in Jökuldalur. Instead we find that the normal polarity intervals in the type sections can both be correlated to Olduvai subchron.
Keywords: Gilsá event, Paleosecular variation, Paleointensity, Matuyama, Iceland, Ar-Ar radiometric dating

1. Introduction

Satellite observations of the geomagnetic field show that it is dominated by a strong dipolar component, which is highly dynamic, changing chaotically in both direction and intensity. These temporal changes, known as geomagnetic secular variation, are thought to reflect both short- and long-term changes in fluid processes in the Earth's core (Johnson and McFadden, 2007). A fundamental assumption in our use of paleomagnetic data, e.g., in plate reconstruction studies is that when observed over geological timescales the secular variation is averaged out, and the time-averaged field (TAF) is a dipole field aligned with the rotation axis, the so called geocentric axial dipole field (GAD) (Hospers, 1954).

Recent paleomagnetic results from high latitudes (>60°) have studied the apparent long-lived hemispheric asymmetry of the magnetic field on time-scales of 10^5 to 10^6 years, contrasting higher and more stable fields in the north with lower average strength and less stable fields in the south (Cromwell et al., 2015, 2013; Lawrence et al., 2009; Tauxe et al., 2004a). However, modern-standard high-latitude paleomagnetic data, especially absolute paleointensity data, of 0.1–5 Ma rocks are sparse (Figure 1a). Only sporadic temporal overlap exists between high-latitude northern and southern paleointensity data for rocks older than 100 kyr and, in particular, for

stable field periods (Figure 1b). Such data are vital in order to sample and characterize high-latitude paleostructures of the radial magnetic field at the Core-Mantle Boundary.

The basaltic lava sequences of Iceland (64–66°N) have been subject of numerous paleomagnetic studies since the early 1950s, but with a majority of studies focusing on stratigraphic mapping and/or extension of the geomagnetic polarity time-scale, sampling 2–5 cores per site (e.g., Helgason and Duncan, 2001; Kristjánsson et al., 1980, 2004; McDougall et al., 1977; Udagawa et al., 1999; Watkins et al., 1975). Other studies have targeted geomagnetic reversals (Camps et al., 2011) or excursions (Jicha et al., 2011; Kristjánsson, 1999), or have focused on the field strength during transitional events (Camps et al., 2011; Goguitchaichvili et al., 1999) or during the last ∼100 kyr (Cromwell et al., 2015; Tanaka et al., 2012). Little work has been done on Icelandic rocks to produce modern-standard PSV and paleointensity data for geomagnetic stable periods for rocks >100 kyr.

We present modern-standard paleomagnetic and $^{40}Ar/^{39}Ar$ radiometric results of ∼0.5–3.1 Ma rocks from Jökuldalur (Figure 1c), including absolute paleointensity and PSV data. We provide stable field strength estimates for the period 1–2 Ma, which allows us to carry out a comparison of high-latitude northern and southern field behavior during this period (cf. Figure 1b). We also present a revised magneto-chronostratigraphy of Jökuldalur, including an examination of the Gilsá event, a short normal polarity subchron inferred to exist around 1.62 Ma (McDougall and Wensink, 1966; Udagawa et al., 1999).

2. Geology and paleomagnetic sampling

The first paleomagnetic studies in Jökuldalur (Figure 1c) were carried out by Wensink (1964a,b) who established the stratigraphy, covering the Brunhes to Gilbert epochs. The approximate time frame and the existence of the Matuyama reversed (R1) and Gauss normal (N2) polarity epochs was later supported by results of K-Ar radiometric dating (McDougall and Wensink, 1966; Watkins et al., 1975). Wensink (1964b) and McDougall and Wensink (1966) established the Olduvai normal subcron in Hnjúksá (HN) (Figure 1c) based on K-Ar dating. They further argued for a second normal polarity event at 1.60 ± 0.05 Ma (termed *Gilsá*) near the top of this section and above the Olduvai subchron. Subsequent resampling of section HN and additional K-Ar radiometric dating, however, indicated no evidence of this second event (Watkins et al., 1975).

In 1993, Udagawa et al. (1999) revisited Jökuldalur and collected samples from 38 lava flows, mainly from the younger part of the valley along Thverá (TH) and Krengilsá (KG) (Figure 1c). Based on paleomagnetic analysis and new K-Ar ages, Udagawa et al. (1999) correlated the lava flows to 0.5–1.8 Ma. They resurrected the idea of the normal Gilsá event around 1.61–1.62 Ma, this time in section KG. However, the reversely magnetized lavas, located stratigraphically below their inferred Gilsá event, were dated at 1.85 ± 0.08 Ma (2σ), i.e. probably within the Olduvai subchron (1.78–1.94 Ma) (cf. Gradstein et al., 2012): The existence of the Gilsá event is therefore debatable.

In 2013 and 2014, we resampled sections HN, KG and TH (Figures 1c and 2). In total, >700 cores were sampled at 51 sites (site average of ∼15

cores). We sampled 42 sites in 2013 together with another 120 sites in Fljótsdalur, east of Jökuldalur (work in progress). Based on stratigraphic remapping of Jökuldalur in 2014, we sampled another three, previously unmapped, sites near the top of section TH (Figure 2: sites THA12, THA13 and THA15). Due to time constraints, we did not sample the few normal polarity sites of section HN near the river, below HN3. These sites are thought to be of Gauss age (McDougall and Wensink, 1966).

Our sampling was mostly restricted to unaltered massive cores of basaltic lavas in well-defined flow units (Figure 2). The sampling was generally carried out over tens of meters to avoid the risk that samples were not *in situ* or hit by lightning strikes. We oriented the samples mainly by using a sun compass (71% of all samples). At sites sampled during cloud cover, we oriented the samples by magnetic compass readings supplemented by bearings to known landmarks. We used the bearings to correct our magnetic measurements for these sites. Hand samples were collected from all sites to deliver new $^{40}Ar/^{39}Ar$ radiometric age determinations.

3. Methodology

3.1. Sample preparation and $^{40}Ar/^{39}Ar$ dating method

We selected 11 basalt samples for new age determinations by the $^{40}Ar/^{39}Ar$ incremental heating method. The samples were selected based on their fidelity for Ar-Ar dating and the need for additional Ar-Ar dating in specific intervals. A detailed description of the sample preparation and dating method is found in Section S1 (Suppl. Mat.).

3.2. Demagnetization experiment

Stepwise alternating-field (AF) and thermal demagnetization experiments were initially conducted on two specimens per site to test the behavior of the rocks to magnetic cleaning. For the AF demagnetization we used a Molspin Tumbling AF Demagnetizer and a DETECH D-2000 High-Performance AF Demagnetizer. The specimens were generally AF-demagnetized in 10–12 steps within applied field magnitudes of 3–200 mT. Thermal demagnetization was carried out using single and dual-chamber paleomagnetic ovens from ASC Scientific. Demagnetization was carried out at ∼12 heating steps until the maximum unblocking temperature was reached. The magnetic measurements were made on an AGICO JR5A spinner magnetometer inside a dynamic Helmholtz cage at Imperial College London.

From the pilot studies, AF magnetic cleaning was chosen as the preferred procedure for processing the specimens; from each site, we subsequently subjected one additional specimen to thermal demagnetization and seven to AF demagnetization, i.e. a total of ten separately oriented specimens were demagnetized from each site. We analysed the demagnetization data using Puffinplot 1.03beta (Lurcock and Wilson, 2012), and determined the direction of the characteristic remanent magnetization (ChRM) by means of principal component analysis (Kirschvink, 1980). Usually seven or more points were used to determine the line. We corrected the ChRM directions for a small post-emplacement tectonic tilt to the west as defined by dip and azimuth of ∼2° and ∼266°, respectively (Wensink, 1964b). Site mean directions were calculated using Fisher statistics (Fisher, 1953) and only directions trending to the origin with a maximum angle of deviation (MAD) <5°. Oc-

casional specimen ChRM directions being significant outliers as compared to otherwise well-grouped site directions were discarded for further analysis (see Section S2, Suppl. Mat. for details). Additional specimens from these sites were subjected to AF magnetic cleaning to replace the misbehaved ones. We note that sedimentary samples from sites HNA15 and HNA14 (hyaloclastites) (Figure 2) were excluded in the further analysis because the samples either broke apart during transport or showed non-ideal behaviour to magnetic cleaning.

3.3. Rock and paleointensity experiment

As part of our pilot paleointensity experiments we carried out a set of rock magnetic measurements to ascertain the magneto-mineralogy and to assess for possible thermal alteration. The results are presented in Section S3 (Suppl. Mat). We used the IZZI modified protocol (Tauxe and Staudigel, 2004) of the Thellier-Thellier paleointensity experiment (Thellier and Thellier, 1959) to estimate intensity. We initially tested two specimens from all sites for their ability to recover the paleointensity. Based on these and the rock magnetic results, we identified sites suitable for further intensity experiments.

Our first pilot study was carried out on 30 specimens in an applied field of 40 μT (field applied along the specimens cylindrical axis). This experiment consisted of a series of 28 IZ and ZI heating steps, three pTRM checks and two pTRM tail checks. Samples were generally heated until $\sim$95% of the NRM was demagnetized. The remainder of the pilot studies as well as subsequent intensity experiments were carried out in an applied field of 30 μT and consisted of series of $\sim$34 heating steps, five pTRM checks and four

pTRM tail checks. In total, we subjected 205 specimens to IZZI intensity experiments. Due to instrumental problems we had to stop two experiments for four weeks. Subsequent measurements from these experiments were suspicious, and measurements related to those specific temperature intervals were deleted before processing the results. All measurements were conducted at Imperial College London.

4. Results

4.1. $^{40}Ar/^{39}Ar$ radiometric dating

In order to detect samples still affected by groundmass alteration remaining after the acid leaching procedure, 29–35 heating steps were carried out for each sample (Figure 3; Figure S1-1, Suppl. Mat.). The number of low temperature heating steps was increased to ensure an effective removal of any remaining alteration and atmospheric contamination. In 14 or fewer low temperature steps, a sufficient amount of discordant gasses were released to allow recognition of horizontal age plateaus with reproducible primary crystallization ages. Between 11 and 29 of the heating steps define the age plateaus that also include from 43% to 100% of the $^{39}Ar_{\kappa}$ gas released. Only one of the eleven groundmasses yielded an age plateau with less than 50% of the total amount of $^{39}Ar_{\kappa}$ gas released. Nine out of eleven inverse isochron intercepts are within error of the 295.5 modern atmospheric ratio of $^{40}Ar/^{36}Ar$. For all experiments the K/Ca value decreases from the low-temperature steps through the age plateau to the high-temperature steps; most likely a result from alteration phases that readily lose gas at low temperatures while argon retentive phases such as groundmass plagioclase and clinopyroxene tend to

degas at high temperatures.

Our approach gave high-precision ages (with nominally 1.3–3.8% 2σ uncertainties, including J-value errors), except for sample THA0 that yielded less argon than the rest. TH-14 gave a plateau age of 1.05 ± 0.04 (95.7% $^{39}Ar_K$) concordant with a total fusion age of 1.02 ± 0.04 Ma, while the inverse isochron age is 0.73 ± 0.21 Ma. The site polarity (normal) and section magnetostratigraphy suggests an age of 1.05 Ma (Jaramillo) rather than 0.73 Ma (Brunhes), and we therefore reject the isochron age for TH-14. Samples KG-2 and HN-13 gave age spectra that suggest modest disturbance with down-stepping ages toward higher temperature steps, likely due to ^{39}Ar recoil, with superimposed argon loss at low temperature steps. However, the plateau and isochron ages are not different from the total fusion ages at 2σ (Table S1-1, Suppl. Mat.). Regardless of the modest complexities in release behaviour and argon loss, the high-resolution incremental heating age analyses on crystalline groundmass samples from Jökuldalur show concordances in plateau, isochron and total fusion ages, indicating that the primary argon reservoirs were not significantly affected by alteration or recoil, and that the K-Ar isotope system has effectively remained closed since the time of eruption. For the age model presented in the Discussion we use the plateau ages for all samples except for KG-2 and HN-13 for which we use the total fusion ages (Figure 2).

The total age range of the eleven new ^{40}Ar/^{39}Ar ages (Figures 2, 3) covered by sites TH17 to HN3 is ∼0.63–3.13 Ma. This age range broadly concurs with the chronostratigraphy established by Udagawa et al. (1999) and McDougall and Wensink (1966). However, important deviations occur,

particularly in section KG; the type section for the Gilsá event (Udagawa et al., 1999) (see Discussion).

4.2. Paleodirections

In Figure 4a, we show representative examples of AF and thermal demagnetization data. In general, remanence resides in a stable single component of magnetization acquired during original cooling. A secondary viscous component (VRM) of much smaller magnitude was often removed by AF demagnetization peak fields of 5–15 mT or temperatures of ∼200°C. In summary, we obtain well-grouped ChRM directions from 49 sites (Table 1), with site mean directions generally being defined by N >10 (N_{min} =7, N_{max} =16), k >200 (k_{min} =76, k_{max} =3584), and $\alpha 95$ <3.5° ($\alpha 95_{max}$ =5.4°), where N is the number of independent data at each site, k is the precision parameter, and $\alpha 95$ is the circle of 95% confidence (Fisher, 1953). Our re-mapping of Jökuldalur in 2014 indicated that some lava flows were drilled twice. Field observations combined with paleomagnetic results (common mean test) suggest that sites TH16/TH17, KG0/KGA0, HNB15/HNC15, and HN10/HN11, respectively, are units that were drilled twice, i.e. only 45 sites of the 49 sites are distinct. The resulting 10 normal and 35 reverse site mean directions yield Declinations (D) and Inclinations (I) of D_{normal} =351.5°, I_{normal} =77.9° and $D_{reverse}$ =176.8°, $I_{reverse}$ =-75.9° (Table 1). The normal and reverse directions pass a bootstrap reversals test (Tauxe, 2010) at the 95% level of confidence, having mean directions inside the confidence regions of each other. This allows the data to be combined to an overall combined mean direction for N =45 sites with a result of D =355.7°, I =76.3°, $\alpha 95$ =3.2 (Table 1) that is not significantly different from the geocentric axial dipole field for Jökuldalur (I =77°)

(Figure 4b).

We also calculated the virtual geomagnetic poles (VGPs) for the N =45 sites. The VGPs distribute around the North Pole (Figure 4c), and the resulting mean paleomagnetic pole ($\bar{\lambda} = 87.8°$, $\bar{\phi} = 224.3°$) is coincident with the North Pole within the 95% confidence limit (Table 1).

4.3. Paleointensity

The Thellier GUI Auto Interpreter (Shaar and Tauxe, 2013) was used for paleointensity analysis. We visually inspected both the Arai and vector-endpoint diagrams as an initial quality check. For specimens that display relatively linear components of magnetization, the minimum number of successive points used for the determinations was fixed to $N \geq 10$. In addition, we adopted a relatively strict set of specimen-level cut-off criteria modified after Cromwell et al. (2015, 2013); Selkin and Tauxe (2000): $FRAC$ >0.78, β <0.1, q >7 and $DRAT$ <10%. Our strategy was then to find the set of threshold values for e.g. MAD and DANG that accepted the most sites with $N \geq 3$ successful intensity estimates per site. We found that MAD <11°, MAD_{anc} <6°, α <4.8° and $DANG$ <8.0 gave good technical results and screened out specimens that we found unreliable.

We used all the intensity estimates accepted at each site at the specimen-level to calculate the site median intensity (B) which is less affected by outliers than the site mean. Given the limited estimates per site ($N = 3 - -9$) we did not filter our results, e.g., by using a certain percentage fraction (or the standard deviation) to set up maximum deviation bounds relative to the site median, and thereby remove what may seem to be outliers. Instead, we report the median intensity for each accepted site along with the minimum

and maximum site intensity values.

We accepted 44 intensity estimates from 16 sites by the specimen-level cut-off criteria (Table 2: upper part). The $FRAC$ used for paleointensity determination ranges from 0.78 to 0.98 with 50% exceeding 0.89, whereas the quality factor q varies from ranges from 7.8 to 27.6 with 50% exceeding 12. We regard these as being data of good technical quality.

In Figure 5a–e we show representative specimen behaviors for accepted field estimates passing all the specimen-level criteria, including Arai curves that are relatively well-behaved and linear (Figure 5a–c) or nearly linear (Figure 5d–e). Examples of rejected specimens are shown in Figure 5f–h. Figure 5f shows an example of specimens that display linear Arai curves, but fail on the $DRAT$ criteria of maximum 10%. Figure 5g shows an example of distinct concave-up behavior, usually interpreted as characteristic of multidomain remanences (Dunlop and Özdemir, 2001). Selecting the low-temperature results in a high-ancient field estimate (61 μT) whereas the high-temperature component results in a low-ancient estimate (12 μT). While both components meet some of the criteria above, they are incompatible with each other. In accordance with Cromwell et al. (2013), we rejected specimens with such behaviour until further constraints can be placed on the reliability of concave-up Arai plots. In Figure 5h, we show an example of a specimen with indication of alteration at 250–425°C. The subsequent Arai curve is relatively linear but fails the $FRAC$ and $DRAT$ criteria. In general, we rejected specimens with such behaviour.

Of the 16 sites, only six sites were accepted by the site-level criteria $N \geq 3$ (Table 2: lower part). The median paleointensity ($\overline{B}$) of our six accepted

site intensities is 41 μT with a median absolute deviation of 3 μT (Table 2), which is less than the present day Iceland field intensity of $\sim$52 μT. The minimum and maximum site intensities are $36\frac{37}{34}$ μT (site KG5) and $55\frac{67}{39}$ μT (site THA4), respectively, i.e. only site THA4 gave intensities comparable to the current intensity. We have added the median intensity estimate ($\overline{B}$ =41μT) to the plot in Figure 1a. Our result is within the range of previously published (non-Holocene; 11 ka – 3.3 Ma) field strength estimates from Iceland of $\sim$31 μT, with minimum and maximum intensities of 12 μT and 78 μT, respectively (Cromwell et al., 2015). We also calculated the median virtual axial dipole moment ($\overline{VADM}$) and the median virtual dipole moment ($\overline{VDM}$) for our six intensity estimates (Table 2). We obtain a $\overline{VADM}$ of 57 ZAm^2 with a median absolute deviation of 3 ZAm^2. The corresponding latitude-independent $\overline{VDM}$ is 60$\pm$5 Am^2.

In Discussion, we compare our high-northern latitude results to high-southern latitude results from Antarctica (Lawrence et al., 2009), using both our own cut-off criteria and the less strict specimen-level cut-off criteria of Lawrence et al. (2009) (see Table S4-1 in Suppl. Mat). Post removal of 11 estimates, considered unreliable, we accepted 84 intensity estimates from 25 sites by the Lawrence et al. (2009) cut-off criteria (see Table S4-2, Suppl. Mat.). Of these, 14 sites pass our $N \geq 3$ site-level criteria, resulting in $\overline{B} = 29 \pm 8$ μT, $\overline{VADM} = 40 \pm 11$ ZAm^2, and $\overline{VDM} = 42 \pm 12$ Am^2. Thus, eight additional sites were accepted using these criteria, resulting in a lower median field estimate. However, if looking solely at the six sites accepted by our preferred criteria (Table 2), $\overline{B}$ increases to 36 ± 6 μT when applying the criteria of Lawrence et al. (2009), i.e. statistically equal to our preferred

estimate of 41±3 μT.

5. Geomagnetic field behaviour

5.1. VGP dispersion and time-averaged inclination

A key objective of time-averaged field (TAF) studies is to determine the dispersion of the site mean directions through time (Johnson et al., 2008), which is assumed to be due to paleosecular variation (PSV). The dispersion can be evaluated quantitatively using VGPs from each distinct site (Table 1) and is traditionally represented by the root mean square angular deviation of VGPs about the Earth's spin axis (Cox, 1969). Here, we used the modified angular standard deviation S_B (Johnson et al., 2008) that corrects for within-site dispersion S_{W_i}.

Using all the data from the 45 sites (∼0.6–3.1 Ma interval), taking the antipodes of the reverse poles, we obtain a dispersion $S_B = 19.9^{\frac{22.3}{17.5}}$ (95% bootstrap and upper and lower confidence bounds). None of our sites are excluded using a standard VGP latitude cut-off of 45° (e.g., Johnson et al., 2008), therefore the VGP dispersion ($S_{B(45°)}$) using this criterion is the same. According to our revised stratigraphic age model (Section 6), 38 of our sites (TH15 to HN9) are of Matuyama age, one site (TH16/TH17) is of Brunhes age and five (HN8–HN3) are of Gauss age (Figure 2). We calculated a VGP dispersion $S_{B(Mat)} = 20.5^{\frac{23.3}{17.8}}$ for our Matuyama age data that is statistically identical to $S_B = 19.9^{\frac{22.3}{17.5}}$ obtained for the $N = 45$ data, normal and reverse data combined. Based on the new Jökuldalur data set we cannot exclude differences in dispersion for the Matuyama as compared to the entire ∼0.6–3.1 Ma age interval.

316 In order to compare with previous results from Iceland, we calculated S_B
317 and $S_{B(45^\circ)}$ for (i) the Jökuldalur data set of Udagawa et al. (1999) and (ii)
318 for a regional Iceland compilation of 1388 site mean VGPs of 0–5 Ma rocks
319 (see Section S5, Suppl. Mat.). These older data sets are based on surveys
320 sampling 2–5 cores per site. We also calculated $S_{B(Mat45^\circ)}$ for these data, i.e.
321 the VGP dispersion for Matuyama age data using a cut-off of 45°. For the
322 Udagawa data set we obtain $S_B = 23.8^{\frac{28.0}{19.9}}$ (38 sites), $S_{B(45^\circ)} = 22.1^{\frac{25.1}{19.5}}$ (37
323 sites) and $S_{B(Mat45^\circ)} = 21.8^{\frac{24.7}{18.9}}$ (35 sites), whereas for the regional Iceland
324 compilation we obtain $S_B = 24.0^{\frac{24.7}{23.2}}$ (1388 sites), $S_{B(45^\circ)} = 22.5^{\frac{23.0}{21.9}}$ (1347
325 sites) and $S_{B(Mat45^\circ)} = 21.4^{\frac{22.2}{20.6}}$ (688 sites). As evident, the VGP disper-
326 sion, S_B, $S_{B(45^\circ)}$ and $_{B(Mat45^\circ)}$, from the older data are ∼4°, 2–3° and 1–2°
327 higher, respectively, than VGP dispersion for the new Jökuldalur data. De-
328 spite having overlapping 95% levels of confidence the means of S_B for this
329 study and the study of Udagawa et al. (1999) lie outside the 95% confidence
330 region of each other and are only just included for $S_{B(45^\circ)}$. For the regional
331 compilation and the new Jökuldalur data set, the means are not included in
332 the 95% levels of confidence of each other in any of the calculations. These
333 results suggest that S_B – and potentially $S_{B(45^\circ)}$ and $_{B(Mat45^\circ)}$ – are signifi-
334 cantly lower for the new Jökuldalur data set as compared to the older data.
335 We speculate that the reduced VGP dispersion is a function of data quality
336 given the high number of successful ChRMs per site (N >10 on average) for
337 the new data. Thus, the within-flow scatter of the new data set, as defined
338 by the $\alpha 95$ values (Table 1), show mean and maximum values, respectively,
339 of 2.7° and 5.4°, with 50% of all $\alpha 95$ values being less than 2.7°. These
340 values are markedly lower than values for the data of Udagawa et al. (1999)

($\alpha 95_{Mean}$ =4.1°, $\alpha 95_{Max}$ =7.4°, 50% of all α95-values <4.0°) and for the Iceland compilation ($\alpha 95_{Mean}$ =6.0°, $\alpha 95_{Max}$ =23.0°, 50% of all α95-values <5.0°). The above comparisons may stress the importance of maximizing the number of cores per site, preferably to produce ∼10 ChRMs per site, and to maximize the percentage of sun measurements, when carrying out paleomagnetic surveys in basaltic rocks at high latitudes. This conclusion conforms with the observations of Johnson et al. (2008) that inclusion of studies with poor quality data or insufficient samples per site is found to increase S_B.

In the following, we focus on the Matuyama which constitutes the main part of our data set. The geomagnetic field during this reverse polarity chron is generally regarded as more dispersive and to show stronger dependence of S_B on latitude as compared to the Brunhes (Johnson et al., 2008); an interpretation that may be evaluated further by adding our high-northern latitude data. In Figure 6 we plot $S_{B(Mat)}$ for Jökuldalur (this study) together with $S_{B(Mat45°)}$ values calculated from global Matuyama age data. The data are plotted against latitude (Jökuldalur at 65°N) together with the expected VGP dispersion versus latitude for Model G (blue line) of McFadden et al. (1988) and for the GAD version of the TK03 statistical model (green line) of Tauxe and Kent (2004). Also shown are the $S_{B(Mat45°)}$ values for the data of Udagawa et al. (1999) and for the Iceland compilation. As evident from Figure 6 the VGP dispersion $S_{B(Mat)}$ from Jökuldalur (this study) overall supports the interpretation of a dependence of S_B on latitude during the Matuyama (e.g., Johnson et al., 2008) in the northern hemisphere when compared to other modern-standard data sets, and to predictions from the two PSV models. Notably, the mean $S_{B(Mat)}$ from our data correlates well with

the trend of Model G of McFadden et al. (1988) but also overlaps with the trend of the TK03 model of Tauxe and Kent (2004) within the 95% confidence levels. Our data therefore show no preference of the two models. We do, however, not observe a clear indication of less dispersive field behavior in the northern hemisphere as compared to the southern hemisphere during the Matuyama as tentatively suggested by Cromwell et al. (2013).

Deviations from a GAD field are often reported as inclination anomalies $\Delta I = I_{obs} - I_{GAD}$, where I_{obs} and I_{GAD} define the observed and predicted (from a GAD field) inclinations (Johnson and McFadden, 2007). A small negative inclination anomaly ($\sim -3°$) was predicted by Johnson et al. (2008) for the Matuyama at 65°N. We obtain a time-averaged inclination anomaly for the 38 Matuyama age data of $\Delta I_{Mat} = -0.91° \frac{2.94}{-4.88}$ (95% confidence limits calculated using a bootstrap technique) that is negligible. In contrast, ΔI_{Mat} for the data of Udagawa et al. (1999) is $-3.42° \frac{0.55}{-7.84}$, i.e. the older data both suggest a higher VGP dispersion and more deviation from a GAD field as compared to the new modern-standard data. The negligible negative inclination anomaly for the Matuyama presented in this study thus provides important high-latitude constraints on the TAF.

5.2. Field strength

Cromwell et al. (2013) presented five field strength estimates from young volcanic rocks (<300 kyr) from Jan Mayen (71°N) located just north of Iceland. They found a high average VADM of 76.8±24.3 ZAm^2. Recently, Cromwell et al. (2015) added another 44, high-quality, field strength estimates from southern Iceland of which 37 estimates are from rocks younger than 400 kyr, six have an age close to the Matuyama/Gauss boundary and

one is of Gauss age. The results of Cromwell et al. (2015) have a median VADM of 48.6±13.9 ZAm^2. By comparing their results with field estimates from Antarctica (Lawrence et al., 2009) over the same time interval, Cromwell et al. (2015, 2013) argue for the possibility of long-lived hemispheric asymmetry, contrasting higher fields in the north with lower average strength in the south. However, this interpretation is hampered by the general lack of field estimates from the high-latitude southern hemisphere (Figure 1a) and by the poor temporal overlap of stable field high-latitude intensity results between the northern and southern hemispheres, in particular for the Matuyama epoch (Figure 1b).

Our new field estimates (Table 2 and Table S4-2) allow us to compare field strength behavior at relatively high-northern latitudes with field strength estimates from Antarctica for the Matuyama. In Figures 7a and 7b we plot 16 recalculated VADMs from Antarctica (Lawrence et al., 2009; Tauxe et al., 2004b), using a site-level selection criteria of N $\geq$3 (this study). The Antarctic VADMs are shown together with the paleomagnetic axial dipole moment model (PADM2M) of Ziegler et al. (2011) for Matuyama down to 2.0 Ma (i.e. 0.78–2.0 Ma); the PADM2M model predicts the geomagnetic field strength since 2.0 Ma and was derived from both absolute and relative global palaeointensity data. In Figure 7a we show the six preferred median VADMs from Jökuldalur (hereafter referred to as Q1-estimates; see Table 2). In Figure 7a we plot the 11 (0.78–2.0 Ma) VADMs that were produced using the less strict specimen-level criteria of Lawrence et al. (2009) (hereafter referred to as Q2-estimates; see Table S4-2, Suppl. Mat.).

The median of the PADM2M dipole moment for the period 0.78–2.0 Ma

is 49±9 ZAm^2. This is slightly lower than the median field strength of our six Q1-estimates of 57±3 ZAm^2 (Table 2, Figure 7a) but statistically equivalent to the median field of the 11 (0.78–2.0 Ma) Q2-estimates of 47±9 ZAm^2. In contrast, the median VADM of the 16 (0.78–2.0 Ma) field estimates from Antarctic is only 39±7 ZAm^2, i.e. significantly lower than our Q1- and Q2-estimates. Hence, our Matuyama age field strength estimates may support the hypothesis of higher field strengths in the northern hemisphere on 10^5–10^6 time-scales (Cromwell et al., 2015, 2013). However, more paleointensity data are needed to confirm the inferred asymmetry, in particular from medium high latitudes at the southern hemisphere and for latitudes >70°N (Figure 1a). Interestingly, the very high-field estimates predicted at the southern hemisphere around 1.36 Ma (106 ZAm^2) are partly reproduced for the northern hemisphere data at site THA4 around 1.37 Ma (Q1-estimate = 76 ZAm^2; Q2-estimate = 63 ZAm^2), indicating high global field strength.

6. Revised magneto-chronostratigraphy of Jökuldalur

In this section we revise the magneto-chronostratigraphy of Jökuldalur based on the 11 new $^{40}Ar/^{39}Ar$ ages (Figure 2) as well as existing radiometric ages. In total, 26 K-Ar radiometric ages have been published from sections TH, KG and HN, indicating an age range of ∼0.5–3.0 Ma (McDougall and Wensink, 1966; Udagawa et al., 1999; Watkins et al., 1975). Based on paleomagnetic and stratigraphic results, we have confidently correlated 19 of these K-Ar ages to our sites together with two previously published $^{40}Ar/^{39}Ar$ ages (Wijbrans and Langereis, 2003). A full description of the site-to-site correlation and a list of reassigned K-Ar ages are shown in Section S6 (Suppl.

Mat.).

The K-Ar based magneto-chronostratigraphy of Jökuldalur (McDougall and Wensink, 1966; Udagawa et al., 1999; Watkins et al., 1975) indicates that a significant hiatus of ∼400–500 kyr is present near the top of section TH. Here, Udagawa et al. (1999) reported an age of ∼0.5 Ma for site TH16/17, whereas the underlying site TH14 was dated at 0.91 Ma. The results of Udagawa et al. (1999) further suggest that (i) the near base of section TH (site TH1; K-Ar age of 1.30 ± 0.06) and the top of section KG (site KG9; K-Ar age of 1.39 ± 0.06) are statistically coeval, (ii) the near base of section KG (site KG0; K-Ar age of 1.85 ± 0.08) is ∼250 kyr older than site HN16 (K-Ar age of 1.60 ± 0.02) at the top of section HN.

The new $^{40}Ar/^{39}Ar$ ages of site TH16/17 of 0.63 ± 0.03 Ma and site TH14 of 1.05 ± 0.04 Ma (Figure 2) support the interpretation of a major hiatus near the top of section TH although the new ages are ∼100 kyr older. The new ages of site THA0 (1.51 ± 0.14 Ma) and of TH1 (1.46 ± 0.04 Ma) as well as of site KG9 (1.49 ± 0.03 Ma) are statistically identical and support a small overlap between sections TH and KG (Figure 2). Finally, the new ages of site KG2 (1.88 ± 0.04 Ma; total fusion age) and site HNC15 (1.83 ± 0.04 Ma) indicate that some overlap exist between the normal polarity intervals in sections KG and HN. The new age of site HN13 (2.26 ± 0.04 Ma; total fusion age) suggests the normal interval in HN is separated from the underlying reverse interval by a hiatus of ∼450 kyr, defined by the sedimentary layer of site HNA14.

In Figure 8a, we plot the 11 new $^{40}Ar/^{39}Ar$ ages together with radiometric ages, confidently correlated to our sites (Table S6-1). All ages are plotted

against cumulative stratigraphic height (CSH) of sections TH, KG and HN. We estimated CSH from the stratigraphic thickness of each site, taking into account the relative age chronology of the sections (Figure 2) and a regional tectonic tilt of 2° to the west (Section 2). From Figure 8a it is evident that several K-Ar ages are up to 200–300 kyr younger than corresponding $^{40}Ar/^{39}Ar$ ages from the same sites (TH17, TH14, TH1, KG9, KG2, HN9) or from stratigraphically younger sites (TH7, TH8, TH10, KG0), probably indicating variable Ar loss. In contrast, the new and published (Wijbrans and Langereis, 2003) $^{40}Ar/^{39}Ar$ ages for sites HNC15 and HN13 are statistically identical.

In the following, we assume that a segmented linear regression age model is a valid first order approximation to intervals of ages versus CSH between inferred hiati, i.e. the volcanic build-up rate is assumed to have remained fairly constant (cf. McDougall et al., 1977; Watkins and Walker, 1977) for the period spanned by sections TH, KG and HN. For the linear regression analysis we used only the $^{40}Ar/^{39}Ar$ ages. We initially calculated a linear regression model for the interval defined by sites KG7 (CSH of ∼236 m) to TH15 (CSH of ∼499 m) (Figure 8b), which contains four new ages and is bounded above and below by major hiati (Figure 2). Figure 8b shows that several K-Ar ages (TH5, TH6, TH9, TH12) support the linear regression model although a majority (e.g., TH1, TH7, TH8, TH11, THA11, KG9) are significantly younger. Next, we assumed that the KG7-TH15 linear regression model is a valid approximation for all volcanic stratigraphic intervals of sections TH, KG and HN. Based on the stratigraphic mapping (Figure 2) and by using the KG7-TH15 regression model, we defined five main strati-

graphic intervals for sections TH, KG and HN; each defined by a linear trend in age versus CSH and bounded above and below by major hiati (Figure 8b). We then calculated an interpolated age for all sites (Figure 8c) using the segmented regression model, and next used this age model to construct a revised magneto-chronstratigraphy for Jökuldalur based on a correlation with the polarity intervals of GTS2012 (Figure 8d).

As evident from Figure 8d sections TH to HN span the Brunhes to Gauss period, that is, ∼0.6–3.1 Ma. We can confidently correlate the previously unmapped normal polarity interval, near the top of section TH (Figure 2), to the Jaramillo subchron at 0.98–1.08 Ma, whereas the reverse polarity intervals, HN9–HN13 and HN3–HN8, near the base of section HN probably belong to Matuyama and a short reverse polarity interval in Gauss around 3.02–3.12 Ma, respectively. We note that the reverse polarity site HN4 was dated at 2.84 ± 0.04 Ma (Figure 8b), i.e. within a Gauss normal polarity interval. We therefore omitted this age in our regression analysis for the HN3-HN8 interval.

In section HN, the normal polarity interval is defined by sites HNC15-HN16 (Figure 2). McDougall and Wensink (1966) suggested this interval contained a single reverse polarity site. Based on K-Ar dating, they correlated the lower normal polarity interval to the Olduvai subchron and the upper interval to a second normal polarity subchron above the older Olduvai subchron. In accordance with the conclusions of Watkins et al. (1975) we find no evidence of a reverse polarity site within the HNC15–HN16 interval (Table 1; Figure 2). Also, the new $^{40}Ar/^{39}Ar$ age of site HNC15 of 1.83 ± 0.04 Ma confirms that the HNC15–HN16 interval belongs to the Oldu-

vai subchron (Figure 8d). The underlying ∼450 kyr long hiatus represented by the hyaloclastites and brecciated tuffs at HNA14 we correlate with the thick hyaloclastite deposit at the base of section KG (Figure 2). The hiatus between sites KG7 and KG6 we correlate with the hyaloclastite below THA0.

In section KG, the normal polarity interval is defined by sites KG2–KG6 (Figure 2). This interval was interpreted as the Gilsá event at ∼1.62 Ma (Udagawa et al., 1999), based on K-Ar ages of 1.62 ± 0.14 Ma and 1.62 ± 0.06 Ma for sites KG2 and KG4 (Table S6-1). However, Udagawa et al. (1999) also report a K-Ar age of 1.85 ± 0.08 Ma for the reverse polarity site KG0 (Table S6-1), below their inferred normal Gilsá event. This age is within the normal polarity Olduvai subchron (Gradstein et al., 2012). Our revised $^{40}Ar/^{39}Ar$ age for site KG2 is 1.88 ± 0.04 Ma (Figure 2), i.e. $>$ 250 kyr older than the K-Ar age reported by Udagawa et al. (1999). We correlate the normal interval of sites KG2–KG6 to the Olduvai subchron (Figure 8d), similar to the HNC15–HN16 interval in section HN (Figure 2). Hence, we find no evidence of a second normal polarity event around 1.62 Ma (i.e. the Gilsá event), neither in section KG (Udagawa et al., 1999) nor in section HN (McDougall and Wensink, 1966).

7. Conclusions

- We present a paleodirectional, paleointensity and magneto-chronostratigraphic study from Jökuldalur, Iceland. We collected >700 cores from 51 sites along three sections.

- New $^{40}Ar/^{39}Ar$ ages are presented from 11 flows. We find the that the drilled lava flows span the age of ∼0.6–3.1 Ma.

- Based on AF and thermal demagnetization experiments, we obtain well-grouped ChRM directions from 45 distinct sites with site mean directions generally being defined by N >10, k >200 and $\alpha 95$ <3.5°. We obtain a mean direction of D =355.7°, I =76.3°, and $\alpha 95$ =3.2 for the N =45 sites that is not significantly different from a GAD field. Also, the mean paleomagnetic pole ($\bar{\lambda} = 87.8°$, $\bar{\phi} = 224.3°$) is coincident with the North Pole within the 95% confidence limits.

- We calculate a VGP dispersion $S_{B(Mat)} = 20.5^{\frac{23.3}{17.8}}$ and an average inclination anomaly $\Delta I = -0.91^{\circ}\frac{2.94}{-4.88}$ for our 38 Matuyama age data. The dispersion $S_{B)}$ overall supports the interpretation of a dependence of S_B on latitude during the Matuyama, while the negligible ΔI suggests little deviation from a GAD field. When comparing to previous results from Jökuldalur and to various Iceland surveys, sampling 2–5 cores per site, the new $S_{B)}$ and ΔI values are lower. We speculate this may be a function of data quality.

- Based on relatively strict cut-off criteria, we present six field strength estimates from Jökuldalur for the period 1.19–1.83 Ma; a period void of high-northern stable field intensity data. The median field intensity of our six estimates is 41±3 μT (median absolute deviation) with corresponding VADM and VDM values of 57±3 ZAm^2 and 60±5 Am^2. By comparing our results to 16 estimates from Antartica (VADM of 39±7 ZAm^2) for the period 0.78–2.0 Ma, we find support of a higher field strength in the northern hemisphere on 10^5–10^6 time-scales. A similar conclusion is reached when using less strict cut-off criteria resulting in

14 field estimates from Jökuldalur.

- Finally, we present a revised magneto-chronostratigraphic model for Jökuldalur. We find no evidence of a second normal polarity event around 1.62 Ma (i.e. the Gilsá event) within the Matuyama.

8. Acknowledgements

We are grateful to Prof. V. Bachtadse for providing drilling equipment. We also thank Drs. P. Riisager, J. Matzka and L. Kristjannson for assisting the field work planning. The project was funded by the Danish Council for Ind. Res. (12-125623) to A. Døssing. M. S. Riishuus was funded by Rannis and by the Icelandic Centre for Research (09021002). R. Supakulopas was funded from the Dev. and Promotion of Sci. and Tech. Talents Proj., Thailand.

9. References

Camps, P., Singer, B., Carvallo, C., Goguitchaichvili, A., Fanjat, G., Allen, B., 2011. The Kamikatsura event and the Matuyama–Brunhes reversal recorded in lavas from Tjörnes Peninsula, northern Iceland. Earth Planetary Science Letters 310 (1), 33–44, doi:10.1016/j.epsl.2011.07.026.

Cox, A., 1969. Confidence limits for the precision parameter κ. Geophysical Journal International 17 (5), 545–549, doi:10.1111/j.1365-246X.1969.tb00257.x.

Cromwell, G., Tauxe, L., Halldórsson, S., 2015. New paleointensity results from rapidly cooled Icelandic lavas: Implications

585 for Arctic geomagnetic field strength. Journal of Geophysical Re-
586 search,Doi:10.1002/2014JB011828.

587 Cromwell, G., Tauxe, L., Staudigel, H., Constable, C., Koppers, A., Ped-
588 ersen, R.-B., 2013. In search of long-term hemispheric asymmetry in the
589 geomagnetic field: Results from high northern latitudes. Geochemistry,
590 Geophysics, Geosystems 14 (8), 3234–3249, doi:10.1002/ggge.20174.

591 Dunlop, D. J., Özdemir, Ö., 2001. Beyond Néels theories: thermal demagne-
592 tization of narrow-band partial thermoremanent magnetizations. Physics
593 of the Earth and Planetary Interiors 126 (1), 43–57, doi:10.1016/S0031-
594 9201(01)00243-6.

595 Fisher, R., 1953. Dispersion on a sphere. Proceedings of the Royal Society
596 of London. Series A. Mathematical and Physical Sciences 217 (1130), 295–
597 305, doi:10.1098/rspa.1953.0064.

598 Goguitchaichvili, A., Prévot, M., Thompson, J., Roberts, N., 1999. An at-
599 tempt to determine the absolute geomagnetic field intensity in Southwest-
600 ern Iceland during the Gauss–Matuyama reversal. Physics of the Earth and
601 Planetary Interiors 115 (1), 53–66, doi:10.1016/S0031-9201(99)00064-3.

602 Gradstein, F., Ogg, J., Schmitz, M., Ogg, G., 2012. The Geologic Time Scale
603 2012 2-Volume Set. Vol. 2. Elsevier.

604 Helgason, J., Duncan, R. A., 2001. Glacial-interglacial history of the
605 Skaftafell region, southeast Iceland, 0–5 ma. Geology 29 (2), 179–182,
606 doi:10.1130/0091-7613(2001).

607 Hospers, J., 1954. Rock magnetism and polar wandering. Nature (173), 1183–
608 1184, doi:10.1038/1731183a0.

609 Jicha, B. R., Kristjánsson, L., Brown, M. C., Singer, B. S., Beard, B. L.,
610 Johnson, C. M., 2011. New age for the Skálamælifell excursion and iden-
611 tification of a global geomagnetic event in the late Brunhes chron. Earth
612 Planetary Science Letters 310 (3), 509–517, doi:10.1016/j.epsl.2011.08.007.

613 Johnson, C., Constable, C., Tauxe, L., Barendregt, R., Brown, L., Coe, R.,
614 Layer, P., Mejia, V., Opdyke, N., Singer, B., et al., 2008. Recent investiga-
615 tions of the 0–5 ma geomagnetic field recorded by lava flows. Geochemistry,
616 Geophysics, Geosystems 9 (4), doi:10.1029/2007GC001696.

617 Johnson, C., McFadden, P., 2007. Time-averaged field and paleosecular vari-
618 ation. Treatise on Geophysics, Geomagnetism Volume, 417–453.

619 Juarez, M., Tauxe, L., Gee, J., Pick, T., 1998. The intensity of the Earth's
620 magnetic field over the past 160 million years. Nature 394 (6696), 878–881,
621 doi:10.1038/29746.

622 Kirschvink, J. L., 1980. The least-squares line and plane and the analysis of
623 palaeomagnetic data. Geophysical Journal International 62 (3), 699–718,
624 doi:10.1111/j.1365-246X.1980.tb02601.x.

625 Kristjánsson, L., 1999. On low-latitude virtual geomagnetic poles in Icelandic
626 basalt lava sequences. Physics of the Earth and Planetary Interiors 115 (2),
627 137–145, doi:10.1016/S0031-9201(99)00072-2.

Kristjánsson, L., Fridleifsson, I., Watkins, N., 1980. Stratigraphy and paleomagnetism of the Esja, Eyrarfjall and Akrafjall mountains, Iceland. Journal of Geophysics 47, 31–42.

Kristjánsson, L., Gudmundsson, A., Hardarson, B., 2004. Stratigraphy and paleomagnetism of a 2.9-km composite lava section in Eyjafjördur, Northern Iceland: a reconnaissance study. International Journal of Earth Sciences 93 (4), 582–595, doi:10.1007/s00531-004-0409-4.

Kuiper, K., Deino, A., Hilgen, F., Krijgsman, W., Renne, P., Wijbrans, J., 2008. Synchronizing rock clocks of Earth history. Science 320 (5875), 500–504, doi:10.1126/science.1154339.

Lawrence, K., Tauxe, L., Staudigel, H., Constable, C., Koppers, A., McIntosh, W., Johnson, C., 2009. Paleomagnetic field properties at high southern latitude. Geochemistry, Geophysics, Geosystems 10 (1), doi:10.1029/2008GC002072.

Lurcock, P. C., Wilson, G. S., 2012. Puffinplot: A versatile, user-friendly program for paleomagnetic analysis. Geochemistry, Geophysics, Geosystems 13, 10.1029/2012GC004098.

McDougall, I., Saemundsson, K., Johannesson, H., Watkins, N., Kristjansson, L., 1977. Extension of the geomagnetic polarity time scale to 6.5 my: K-Ar dating, geological and paleomagnetic study of a 3,500-m lava succession in western Iceland. Geological Society of America Bulletin 88 (1), 1–15, 10.1130/0016-7606(1977)88¡1:EOTGPT¿2.0.CO;2.

McDougall, I., Wensink, H., 1966. Paleomagnetism and geochronology of the Pliocene-Pleistocene lavas in Iceland. Earth and Planetary Science Letters 1 (4), 232–236, doi:10.1016/0012-821X(66)90075-6.

McFadden, P., Merrill, R., McElhinny, M., 1988. Dipole/quadrupole family modeling of paleosecular variation. Journal of Geophysical Research 93 (B10), 11583–11588, doi:10.1029/JB093iB10p11583.

Opdyke, N. D., Kent, D. V., Huang, K., Foster, D. A., Patel, J., 2010. Equatorial paleomagnetic time-averaged field results from 0–5 Ma lavas from Kenya and the latitudinal variation of angular dispersion. Geochemistry, Geophysics, Geosystems 11 (5), doi:10.1029/2009GC002863.

Panaiotu, C., Visan, M., Tugui, A., Seghedi, I., Panaiotu, A., 2012. Palaeomagnetism of the South Harghita volcanic rocks of the East Carpathians: implications for tectonic rotations and palaeosecular variation in the past 5 Ma. Geophysical Journal International 189 (1), 369–382, doi:10.1111/j.1365-246X.2012.05394.x.

Selkin, P. A., Tauxe, L., 2000. Long-term variations in palaeointensity. Philosophical Transactions of the Royal Society of London A: Mathematical, Physical and Engineering Sciences 358 (1768), 1065–1088.

Shaar, R., Tauxe, L., 2013. Thellier GUI: An integrated tool for analyzing paleointensity data from Thellier-type experiments. Geochemistry, Geophysics, Geosystems 14 (3), 677–692, doi:10.1002/ggge.20062.

Tanaka, H., Hashimoto, Y., Morita, N., 2012. Palaeointensity determinations

672 from historical and Holocene basalt lavas in Iceland. Geophysical Journal
673 International 189 (2), 833–845, 10.1111/j.1365-246X.2012.05412.x.

674 Tauxe, L., 2010. Essentials of paleomagnetism. University of California Press.

675 Tauxe, L., Gans, P., Mankinen, E. A., 2004a. Paleomagnetism and $^{40}Ar/^{3}9Ar$
676 ages from volcanics extruded during the Matuyama and Brunhes Chrons
677 near McMurdo Sound, Antarctica. Geochemistry, Geophysics, Geosystems
678 5 (6), doi:10.1029/2003GC000656.

679 Tauxe, L., Gee, J., Steiner, M., Staudigel, H., 2013. Paleointensity results
680 from the Jurassic: New constraints from submarine basaltic glasses of
681 ODP Site 801C. Geochemistry, Geophysics, Geosystems 14 (10), 4718–
682 4733, doi:10.1002/2013GC004704.

683 Tauxe, L., Kent, D. V., 2004. A simplified statistical model for the geomag-
684 netic field and the detection of shallow bias in paleomagnetic inclinations:
685 was the ancient magnetic field dipolar? Timescales of the Paleomagnetic
686 field, Geophysical Monograph Series 145, 101–115Doi:10.1029/145GM08.

687 Tauxe, L., Luskin, C., Selkin, P., Gans, P., Calvert, A., 2004b. Paleomagnetic
688 results from the Snake River Plain: Contribution to the time-averaged field
689 global database. Geochemistry, Geophysics, Geosystems 5 (8).

690 Tauxe, L., Staudigel, H., 2004. Strength of the geomagnetic field in the
691 Cretaceous Normal Superchron: New data from submarine basaltic glass
692 of the Troodos Ophiolite. Geochemistry, Geophysics, Geosystems 5 (2),
693 doi:10.1029/2003GC000635.

694 Thellier, E., Thellier, O., 1959. Sur l'intensité du champ magnétique terrestre
695 dans le passé historique et géologique. Annales de Geophysique 15, 285–
696 376.

697 Udagawa, S., Kitagawa, H., Gudmundsson, A., Hiroi, O., Koyaguchi, T.,
698 Tanaka, H., Kristjansson, L., Kono, M., 1999. Age and magnetism of
699 lavas in Jökuldalur area, Eastern iceland: Gilsá event revisited. Physics
700 of the Earth and Planetary Interiors 115 (2), 147–171, doi:10.1016/S0031-
701 9201(99)00073-4.

702 Watkins, N., Walker, G., 1977. Magnetostratigraphy of eastern Iceland.
703 American Journal of Science 277 (5), 513–584.

704 Watkins, N. D., Kristjansson, L., McDougall, I., 1975. A detailed paleomag-
705 netic survey of the type location for the Gilsa geomagnetic polarity event.
706 Earth and Planetary Science Letters 27 (3), 436–444, doi:10.1016/0012-
707 821X(75)90063-1.

708 Wensink, H., 1964a. Paleomagnetic stratigraphy of younger basalts and inter-
709 calated Plio-Pleistocene tillites in Iceland. Geologische Rundschau 54 (1),
710 364–384.

711 Wensink, H., 1964b. Secular variation of earth magnetism in Plio-Pleistocene
712 basalts of eastern Iceland. Geologie en Mijnbouw 43, 403–413.

713 Wijbrans, J., Langereis, C., 2003. Elusive Gilsa: Finally laid to rest in north-
714 east Iceland. In: EGS-AGU-EUG Joint Assembly. Vol. 1. p. 11595.

715 Ziegler, L., Constable, C., Johnson, C., Tauxe, L., 2011. PADM2M: a pe-
716 nalized maximum likelihood model of the 0–2 Ma palaeomagnetic axial

Figures and Tables

469

Table 1: Jökuldalur Paleodirectional Site Statistics

Site	Altitude (m)	SLat (°N)	SLon (°E)	$n_l(n_p)/N$	Dec (°)	Inc (°)	k	α95	VGP Lat	VGP Lon	dp/dm	Polarity	Age (Ma)
TH16	607	65.13987	-15.57405	10/10	305.4	76.2	638.2	1.9	67.2	276.4	3.3/3.5	N	0.56±0.06$^{\diamond\diamond}$
TH17	592	65.13630	-15.57320	10/12	304.6	70	154.4	3.9	61.0	258.8	5.8/6.7	N	0.63±0.03$^{\diamond}$
TH15	597	65.14237	-15.56368	11/12	156.3	-66.3	217.7	3.1	-69.4	33.3	4.2/5.1	R	
THA15^{ns}	582	65.14236	-15.56258	9/18	354.8	69.4	306.8	2.9	77.6	179.2	4.3/5.0	N	
TH14	577	65.14232	-15.56065	8/10	339.7	70.4	1009.5	1.7	75.4	217.7	2.6/3.0	N	1.05±0.04$^{\diamond}$
TH13	535	65.12205	-15.53512	12/12	149.4	-76.2	336.5	2.4	-76.9	83.2	4.1/4.4	R	
THA13^{ns}	534	65.12716	-15.53208	12/14	127.9	-75.9	76.5	5	-68.0	94.2	8.5/9.2	R	
THA12^{ns}	534	65.12714	-15.53144	10/14	138.7	-73.7	80.9	5.4	-70.5	77.6	8.7/9.7	R	
TH12	520	65.12938	-15.52793	11/13	198.5	-61.7	265.2	2.8	-65.5	310.4	3.4/4.3	R	
THA11	513	65.12940	-15.52788	11/12	185.4	-54.2	279.7	2.7	-59.5	335.7	2.7/3.8	R	1.18±0.08$^{\diamond\diamond}$
TH11	508	65.12765	-15.52680	10/11	194.4	-61.5	234.2	3.2	-66.1	317.7	3.8/4.9	R	1.10±0.06$^{\diamond\diamond}$
TH10	505	65.12713	-15.52488	10/12	164.2	-71.7	247.3	3.1	-78.5	33.6	4.8/5.4	R	0.91±0.10$^{\diamond\diamond}$
TH9	501	65.12708	-15.52487	8/11	172.7	-73.4	591.4	2.3	-83.2	17.8	3.7/4.1	R	1.19±0.18$^{\diamond\diamond}$
TH8	498	65.12717	-15.52478	10/12	175.4	-78.7	347.8	2.6	-86.4	136.1	4.7/4.9	R	1.02±0.12$^{\diamond\diamond}$
TH7	489	65.12745	-15.52488	10/10	132.3	-79.8	194.8	3.5	-71.7	111.8	6.4/6.6	R	0.98±0.06$^{\diamond\diamond}$
TH6	490	65.12070	-15.51982	11/11	202.3	-68.2	525.4	2	-72.1	294.0	2.8/3.4	R	1.26±0.04$^{\diamond\diamond}$
TH5	467	65.11755	-15.51992	11/11	161.3	-72	225.5	3	-77.9	41.0	4.7/5.4	R	1.26±0.04$^{\diamond\diamond}$
THA4	422	65.11588	-15.51827	12/12	94.9	-86.7	260.5	2.7	-64.9	149.0	5.3/5.4	R	1.22±0.12$^{\diamond\diamond}$
TH4	409	65.11458	-15.51762	10/12	155.6	-85.6	107.9	4.7	-72.8	152.1	9.2/9.3	R	
TH3	415	65.11423	-15.51623	10/16	118.5	-89.2	1404.2	1.3	-65.9	161.0	2.6/2.6	R	
TH2	403	65.11318	-15.51393	10/10	89.3	-86.7	882.1	1.6	-64.2	149.2	3.2/3.2	R	1.26±0.14$^{\diamond\diamond}$
TH1	390	65.11277	-15.51303	12/12	191.8	-77.8	333.3	2.4	-85.0	231.6	4.2/4.5	R	1.46±0.04$^{\diamond}$
TH0^{ns}	349	65.10895	-15.51377	9/9	253.5	-81.2	295.3	3	-64.4	205.7	5.6/5.8	R	
THA0	351	65.10815	-15.51725	11/11	201	-79.2	487.1	2.1	-81.0	218.5	3.8/3.9	R	1.51±0.14$^{\diamond}$
KG9	507	65.17520	-15.31460	10/10	162.3	-59.1	376.5	2.5	-62.7	15.3	2.78/3.72	R	1.49±0.03$^{\diamond}$
KG8	505	65.17522	-15.31432	10/10	171.6	-59.7	498.4	2.2	-64.9	359.9	2.46/3.26	R	
KG7	496	65.17485	-15.31370	12/12	160.7	-65.5	320.5	2.4	-69.7	24.6	3.21/3.95	R	
KG6	478	65.17405	-15.31185	9/9	50	84.1	612.7	2.1	70.6	12.6	4.04/4.1	N	
KG5	462	65.17332	-15.31030	9/10	34.6	85.3	218.1	3.5	72.1	2.0	6.85/6.92	N	
KG4	451	65.17300	-15.31008	13/13	353.8	84.5	133.6	3.6	76.0	339.9	7.01/7.1	N	1.62±0.06$^{\diamond\diamond}$
KG3	447	65.17287	-15.30978	11/11	341.4	69.2	215.3	3.1	74.4	210.7	4.52/5.31	N	
KG2	428	65.17223	-15.30902	11/11	21.4	63.3	285.2	2.7	66.5	124.2	3.37/4.27	N	1.97±0.05$^{\diamond}$
KG1	422	65.17195	-15.30845	10/12	294.9	-75.3	261.2	3	-46.1	202.2	5.01/5.48	R	
KG0	401	65.17073	-15.30758	8/9	171.9	-61.2	214.9	3.8	-66.6	0.0	4.46/5.81	R	1.85±0.08$^{\diamond\diamond}$
KGA0^{ns}	372	65.17000	-15.30588	9/10	181.8	-63.9	178.9	3.9	-70.3	341.0	4.88/6.14	R	
HN16	532	65.24460	-15.22970	10/11	333.2	75.2	723.5	1.8	77.9	252.5	3.01/3.29	N	1.60±0.02$^{\diamond\diamond}$
HNB15	497	65.24450	-15.22448	9/11	98.8	88.1	526.6	2.2	64.4	353.5	4.48/4.48	N	
HNC15	482	65.24437	-15.22238	8/10	90	88.2	1058.6	1.7	65.0	353.1	3.4/3.4	N	1.83±0.04$^{\diamond}$
HN13	458	65.24422	-15.21958	11/12	195	-62.6	635.6	1.8	-67.2	316.0	2.22/2.84	R	2.33±0.06$^{\diamond}$
HN12^{ns}	446	65.24405	-15.21760	10/11	169.4	-72.8	319	2.7	-81.4	25.3	4.29/4.82	R	
HN11	437	65.24392	-15.21622	10/11	209.1	-85.9	707	1.8	-72.0	177.8	3.58/3.61	R	
HN10^{ns}	422	65.24368	-15.21540	10/11	213.2	-83.8	449.1	2.3	-74.1	189.9	4.41/4.49	R	
HN9^{ns}	406	65.24377	-15.21397	11/11	239.7	-84.4	283.1	2.7	-68.7	192.2	5.28/5.36	R	2.33±0.03$^{\diamond}$
HN8^{ns}	367	65.24336	-15.21147	9/10	207.3	-67.5	2602.1	1	-69.5	288.2	1.4/1.68	R	
HN7^{ns}	360	65.24333	-15.21126	10/10	192.1	-67.5	254.1	3	-73.8	316.1	4.22/5.06	R	
HN6	350	65.24335	-15.21074	16/18	208	-79.1	419	1.8	-78.6	223.2	3.26/3.43	R	
HN5^{ns}	325	65.24358	-15.20934	7/10	161.5	-79.7	3584.7	1	-81.6	117.0	1.84/1.93	R	
HN4^{ns}	309	65.24347	-15.20743	11/12	170.2	-79.8	335.9	2.5	-83.8	132.9	4.56/4.77	R	2.84±0.04$^{\diamond}$
HN3^{ns}	305	65.24334	-15.20719	9(3)/10	135.9	-80	321	2.9	-73.0	112.6	5.4/5.64	R	3.13±0.08$^{\diamond}$
Mean (all)		65.17	-15.45	45	355.7	76.3	44.8	3.2	87.8	224.3	5.5/5.9		
Normal		65.18	-15.37	10	351.5	77.9	54.6	6.6	86.2	283.5	11.7/12.4		
Reverse		65.17	-15.52	35	176.8	-75.9	42.0	3.8	87.7	203.0	6.5/7.0		

Site: site names of this study ("ns" following the site name denotes sites sampled during cloudy conditions without sun orientations). Altitude: GPS-altitudes in meters. SLat/Slon and Dec/Inc: site latitude/longitude and mean site declination/inclination in geographic coordinates, respectively. n_l: Total number of best-fit lines (including planes, n_p) used in site mean calculations. N: Total number of samples treated from each site. k: Estimate of the Fisher (1953) precision parameter, α95 is the Fisher (1953) circle of 95% confidence. VGP Lat/Lon: Virtual geomagnetic poles together with 95% confidence angles in parallel and meridian dp/dm. N/R in the "Polarity" column refer to normal and reverse polarities, respectively. Age$^{\diamond}$: ^{40}Ar/^{39}Ar radiometric ages (this study). Age$^{\diamond\diamond}$: Reassigned K-Ar ages from previous studies (see text). All ages are with 2σ error. The lower part of the table shows the mean paleodirectional statistics.

Table 2: Statistics for accepted paleointensity results at the specimen-level (upper) and site-level (lower).

Site	Specimen	T_{min}/T_{max}/n	FRAC	DRAT	MAD	MAD_{anc}	α	β	q	DANG	B	VADM	VDM
TH17	TH17B2	0/520/14	0.88	9.64	6.04	3.29	2.44	0.07	13.66	3.22	40	56	60
TH10	TH10E2	250/590/15	0.84	2.97	5.56	2.87	1.04	0.05	18.26	1.39	41	57	60
TH10	TH10H2	100/560/14	0.92	9.73	5.44	2.22	1.1	0.03	27.59	1.31	24	33	35
TH10	TH10M2	300/572/12	0.79	7.02	8.71	4.36	1.3	0.05	14.77	1.7	40	56	59
TH10	TH10N1	300/572/12	0.8	5.73	9.65	4.79	1.83	0.09	8.48	2.38	43	60	63
TH9	TH9H1	150/590/15	0.94	3.24	5.86	2.56	0.34	0.03	23.34	0.42	45	62	65
TH8	TH8E2	350/590/13	0.84	5.81	3.79	1.89	0.67	0.06	12.62	0.88	53	74	72
TH8	TH8i1	100/572/16	0.89	8.71	9.42	3.14	1.51	0.05	11.97	1.69	53	74	72
TH7	TH7H2	0/590/18	0.94	4.98	9.18	4.11	1.96	0.04	21.38	2.4	43	60	58
TH7	TH7J1	150/590/15	0.91	6.07	9.74	4.33	3.31	0.07	12.34	3.98	40	56	54
TH7	TH7K2	200/570/14	0.81	3.52	10.24	4.47	2.33	0.05	14.17	2.81	32	44	43
TH7	TH7i1	0/590/18	0.94	4.17	8.87	3.71	0.21	0.04	18.27	0.26	41	57	55
THA4	THA4B2	0/590/19	0.97	5.08	5.99	3.13	1.2	0.04	19.57	1.62	61	85	79
THA4	THA4C1	0/572/17	0.97	6.12	5.46	2.57	0.85	0.07	11.94	1.08	67	93	87
THA4	THA4K1	100/520/12	0.8	9.49	10.36	3.96	0.41	0.06	11.2	0.47	53	74	69
THA4	THA4L2	150/540/12	0.83	9.79	9.44	4.27	2.98	0.08	9.29	3.62	39	54	51
THA4	THA4O1	150/560/12	0.84	8.31	8.44	4.07	3.61	0.06	13.34	4.44	55	76	71
TH2	TH2J1	100/560/15	0.82	4.65	3.23	2.3	1.06	0.1	10.28	1.85	26	36	34
TH1	TH1K2	200/590/16	0.78	3.88	5.77	2.88	2.36	0.08	9.28	2.96	54	75	74
TH1	TH1N1	200/580/14	0.79	6.37	7.67	3.59	1.21	0.09	8.33	1.53	45	62	62
TH1	TH1R2	100/560/15	0.92	8.92	6.17	2.65	2.18	0.05	16.86	2.6	33	46	45
THA0	THA0D2	100/500/12	0.91	3.42	4.46	4.47	4.4	0.04	19.33	7.19	22	31	30
THA0	THA0M1	0/500/13	0.91	9.71	5.96	3.86	4.76	0.04	18.69	6.16	22	31	30
KG8	KG8E2	150/570/15	0.89	9.67	9.21	4.31	3.63	0.04	18.51	4.43	13	18	22
KG5	KG5B2	150/570/13	0.86	0.85	5.74	4	4.15	0.08	9.24	5.76	36	50	47
KG5	KG5D1	0/560/13	0.96	6.49	10.67	5.08	3.11	0.1	9.59	3.88	34	47	44
KG5	KG5F2	150/570/14	0.89	4.88	6.78	3.53	3.48	0.1	8.62	4.36	37	51	48
KG5	KG5H2	0/570/16	0.94	1.99	6.97	3.53	3.69	0.1	9.38	4.55	37	51	48
KG5	KG5i2	0/572/16	0.98	6.26	9.68	4.7	1.99	0.09	10.01	2.54	35	49	46
KG4	KG4I2	0/570/16	0.91	4.03	4	2.13	2.53	0.09	9.84	3.12	34	47	45
KG4	KG4K1	0/560/14	0.89	4.18	4.97	2.93	3.43	0.08	10.4	4.37	34	47	44
KG3	KG3A2	150/570/15	0.87	2.85	6.28	2.95	3	0.07	11.8	3.62	49	68	74
KG3	KG3F2	150/570/14	0.8	6.82	6.19	2.75	2.36	0.07	10.93	2.83	51	71	77
KG3	KG3G1	0/560/15	0.9	7.01	6.37	2.71	3.16	0.09	10.03	3.67	42	58	64
KG3	KG3H2	0/580/16	0.96	10	5.63	2.87	1.67	0.1	9.16	2.17	23	32	35
KG3	KG3I1	0/560/14	0.84	3.02	6.29	2.99	2.34	0.09	10.96	2.88	35	49	53
KG3	KG3L2	300/570/10	0.8	1.26	5.98	3.28	3.54	0.09	7.82	4.46	53	74	80
KG3	KG3M2	150/560/14	0.79	5.59	4.5	1.71	2.04	0.05	14.72	2.3	32	44	49
KG3	KG3N2	0/520/14	0.81	7.25	4.78	1.73	2.17	0.06	10.8	2.42	40	56	61
KG3	KG3O1	100/540/14	0.81	8.46	8.96	3.5	4.41	0.05	13.02	4.99	45	62	68
KG3	KG3P1	0/540/13	0.84	9.85	4.34	1.59	0.96	0.09	7.91	1.1	42	58	64
KG2	KG2R1	0/570/15	0.84	4.9	9.33	2.62	2.96	0.06	8.87	3.18	38	53	62
HN16	HN16K2	0/540/12	0.82	4.62	7.79	4.06	2.37	0.09	9.69	3.11	31	43	44
HN11	HN11G1	100/580/16	0.89	5.52	6.77	2.71	1	0.03	21.85	1.18	58	80	76

Site	SLat (°N)	SLon (°E)	N	Age (Ma)	$\overline{B}$	B^{upper}	B_{lower}	$\overline{VADM}$	$VADM^{upper}$	$VADM_{lower}$	$\overline{VDM}$	VDM^{upper}	VDM_{lower}
TH10	65.12713	-15.52488	4	1.19±0.04♠	40	43	24	56	60	33	59	63	35
TH7	65.12745	-15.52488	4	1.22±0.04♠	40	43	32	56	60	44	54	58	43
THA4	65.11588	-15.51827	5	1.37±0.04♠	55	67	39	76	93	54	71	87	51
TH1	65.11277	-15.51303	3	1.46±0.04	45	54	33	62	75	46	62	74	45
KG5	65.17332	-15.31030	5	1.80±0.03♠	36	37	34	50	51	47	47	48	44
KG3	65.17287	-15.30978	9	1.83±0.03♠	42	53	23	58	74	32	64	80	35
All sites	65.12857	-15.45429	6	~1.19–1.83	41±3			57±3			60±5		

N: Number of specimens used to calculate site median intensity after meeting the specimen-level cut-off criteria listed in Section 4.3 and the N ≥3 site-level criteria. B: Field strength (μT). VADM: Virtual axial dipole moment (ZAm^2). VDM: Virtual dipole moment (Am^2). $\overline{B}$, $\overline{VADM}$ and $\overline{VDM}$ are median values given with median absolute deviation. Age for site THA0 is new Ar-Ar ages (this study). Ages marked with ♠ are interpolated model ages based on 1st order segmented regression analysis of new and published Ar-Ar ages (see text).

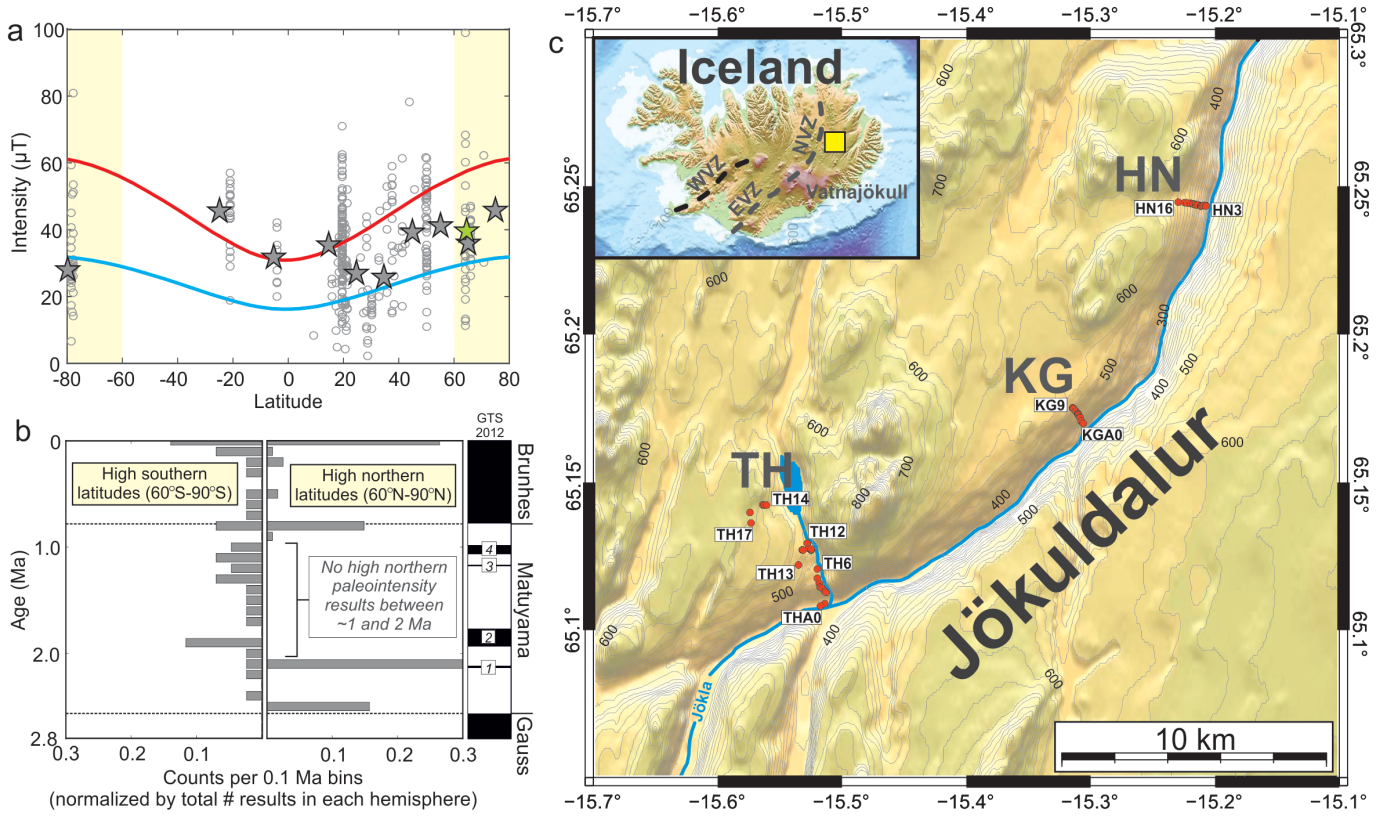


Figure 1: (a) Site-level paleointensity data (0–5 Ma) passing N ≥3 site-level criteria (downloaded from the PINT database at http://earth.liv.ac.uk/pint/). Data are plotted against latitude, and median values for 10° bins are shown as grey stars. Green star: Median paleointensity obtained from Jökuldalur (this study; 41 μT). Predicted values for the present dipole moments of 80 ZAm^2 is shown as red line and for the long-term average field of 42 ZAm^2 ((5-160 Ma, Juarez et al., 1998) and (0-140 Ma, Tauxe et al., 2013)) as blue line. (b) Summary histograms of published field strength estimates. Notice the lack of high-northern data between 1 and 2 Ma. (c) Topographic map of Jökuldalur. Red dots: Location of drill sites (this study) along sections TH (Thverá), KG (Krengilsá) and HN (Hnjúksá). Inset: Topographic map of Iceland. Black dotted lines show location of the main volcanic rift zones. Yellow box: Outline of the area in the main map. Abbreviations: EVZ, Eastern Volcanic Zone; NVZ, Northern Volcanic Zone; WVZ, Western Volcanic Zone.

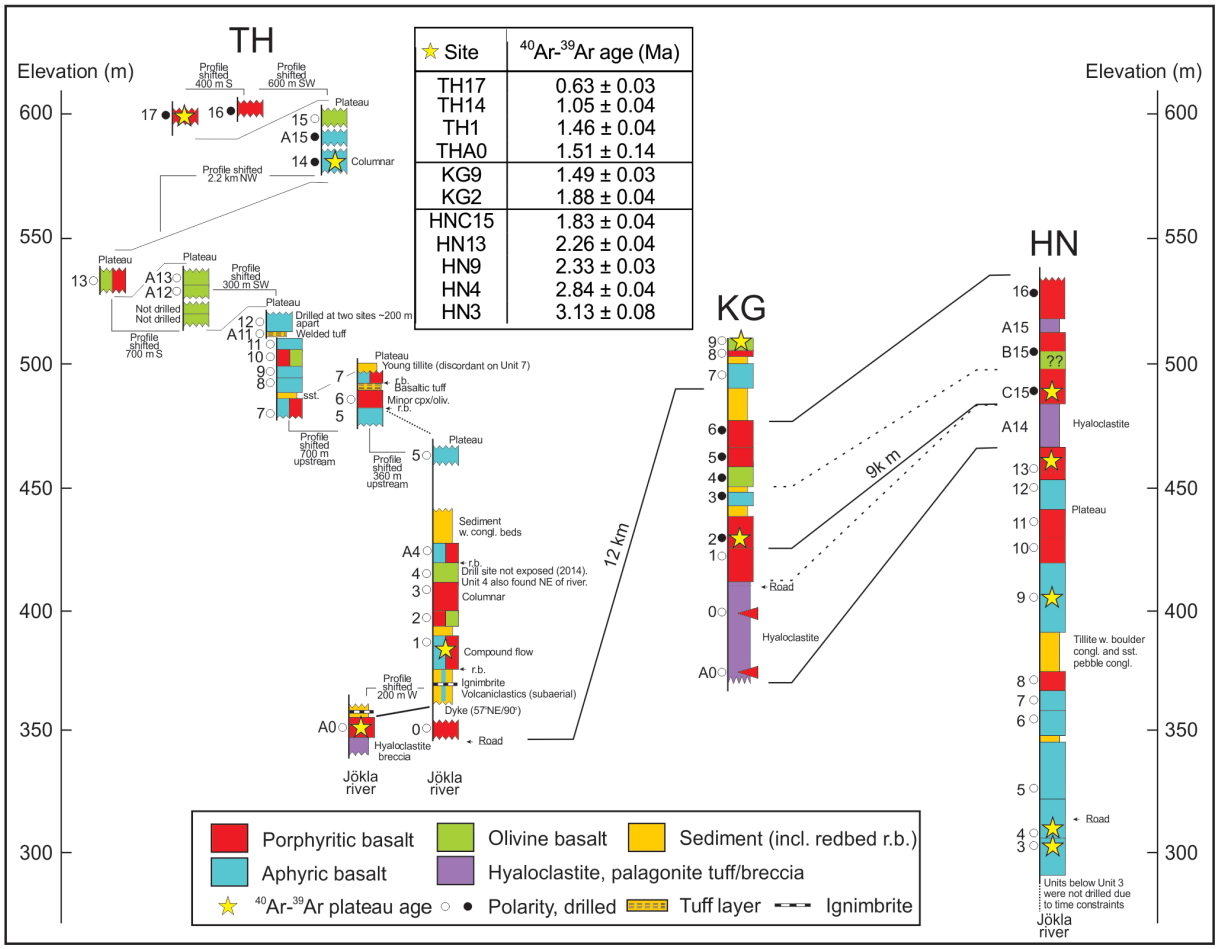


Figure 2: Updated stratigraphy of sections TH, KG and HN. For location, see Figure 1c. Labels to the left are site labels (this study). White(black) filled circles are magnetic reverse(normal) polarity. Yellow stars: New $^{40}Ar/^{39}Ar$ ages (this study). The ages for KG2 and HN13 are total fusion ages (see text). Note the normal polarity intervals in sections KG and HN. The normal polarity interval in section KG was interpreted as the Gilsá event by Udagawa et al. (1999). We correlate both the normal polarity intervals in sections KG and HN to the Olduvai subchron (see text).

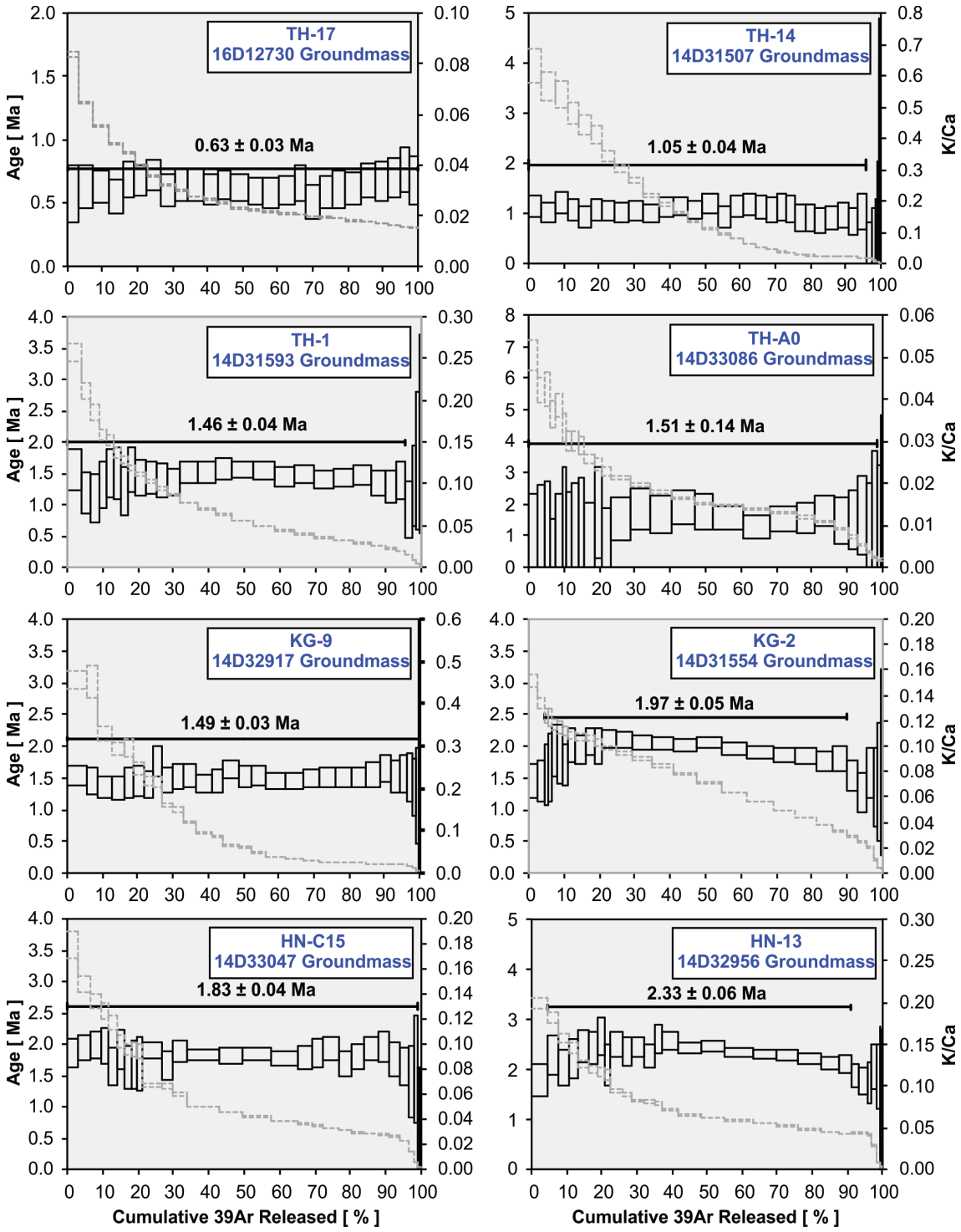


Figure 3: High-resolution incremental heating $^{40}Ar/^{39}Ar$ age spectra on groundmass separates of subaerial basalt samples from profiles TH, KG and HN. The age spectra are presented in stratigraphic order from young to old in the lava pile. The $^{40}Ar/^{39}Ar$ ages are weighted age estimates with errors reported at the 95% confidence level, including 0.2-0.3% standard deviations in the J-value. All samples were monitored against FCT sanidine (28.201 ± 0.023 Ma, 1σ) as calibrated by Kuiper et al. (2008). Solid black lines are $^{40}Ar/^{39}Ar$ ages and stippled gray lines are K/Ca values. Data are listed in Table S1-1 (Suppl. Mat.).

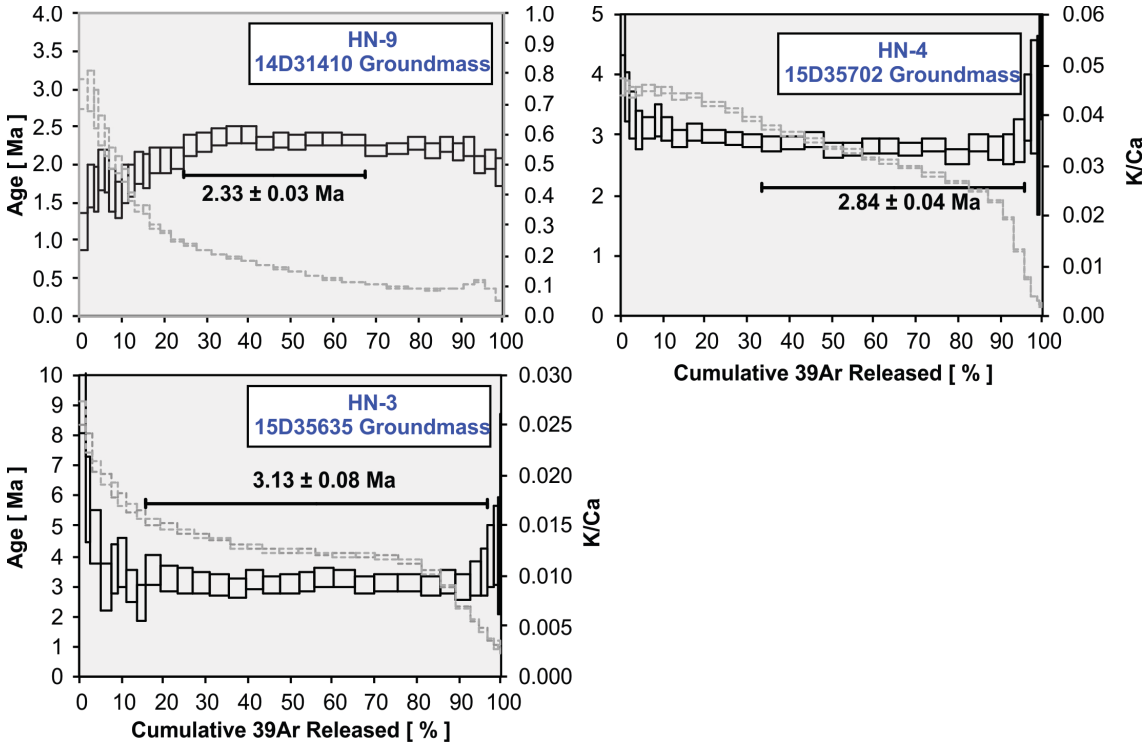


Figure 3: Continued

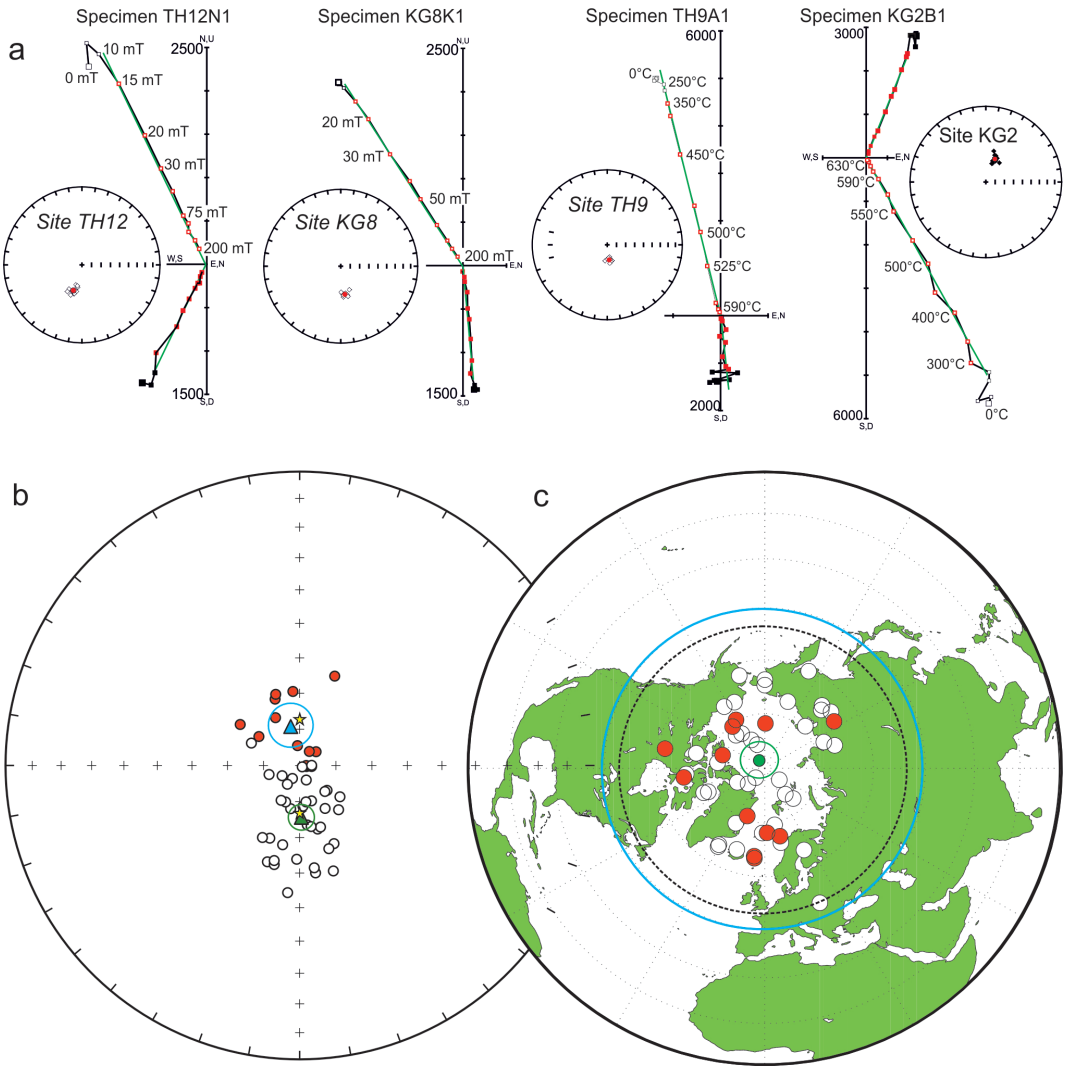


Figure 4: (a) Representative Zijderveld diagrams of AF (alternating-field) and thermal demagnetization experiments. Values along axes are magnetization (mA/m). Closed(open) circles are the horizontal(vertical) plane projection of the directional vector. Inset figures: Site mean directions for the corresponding sites. Red squares mark the site means. (b) Equal area projection of site-mean directions for Jökuldalur. Filled (open) circles plot on the lower (upper) hemisphere. Grand mean directions (triangles) with $\alpha 95$ confidence cones for normal (blue circle) and reversed (green circle) sites. Yallow stars: Expected directions from a GAD field. (c) VGP positions for all sites. Dotted black circle is at 50.2° latitude (Vandamme). Full blue circle is at 45° latitude. Filled (open) circles are northern hemisphere (antipodes of southern hemisphere) VGP positions. Filled green circle: grand mean VGP (paleomagnetic pole) for the 45 distinct sites with 95% confidence cone that encompasses the North Pole.

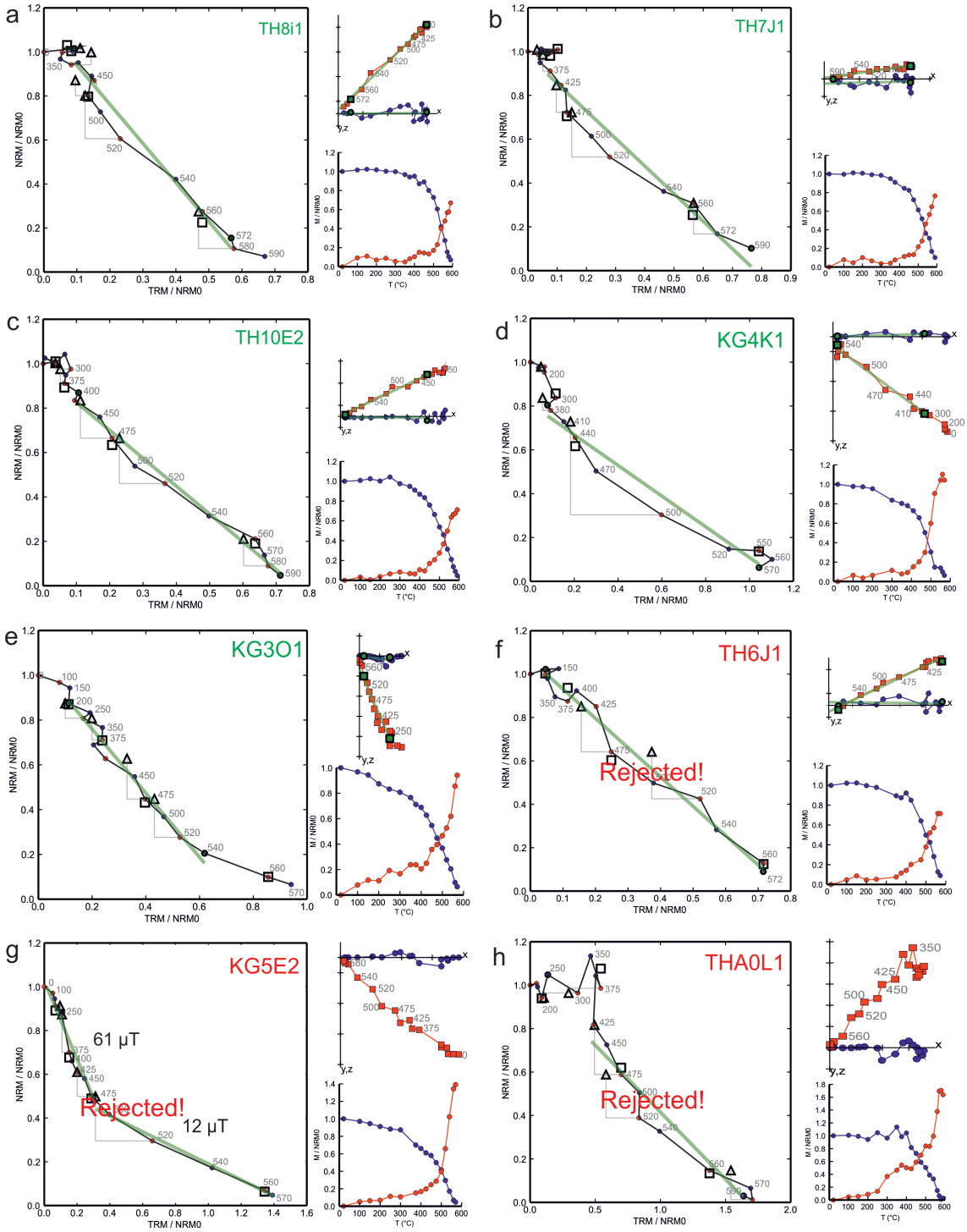


Figure 5: Representative paleointensity results displayed by Arai plots, vector end-point diagrams and NRM-decay/TRM-growth curves for each specimen. (a)–(e) Accepted and (f)–(h) Rejected specimen examples using our preferred cut-off criteria listed in Section 4.3. In (g): Two paleointensity estimates are shown (high and low temperature components); each of which could be valid under certain selection criteria. For our preferred intensity estimates in Table 2 (Q1-estimates; see text) we rejected specimens showing such behavior. pTRM checks are shown as open triangles, pTRM tail-checks as open squares, zero-field/in-field (ZI) temperature steps shown as red dots and IZ steps shown in blue. The green line is the least-squares component for selected temperature steps generated by Thellier GUI Auto Interpreter (Shaar and Tauxe, 2013). Vector end-point diagrams are x-y (x-z) projections of the NRMs in the specimen coordinate system, where x axis is rotated to the direction of the NRM in the x-y plane. NRM-decay curves are shown in blue, TRM-acquisition curves in red.

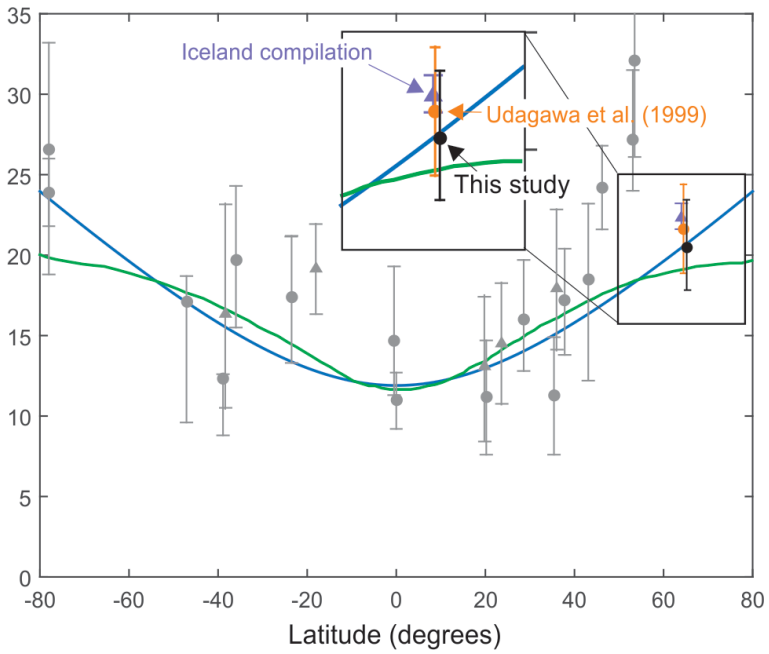


Figure 6: VGP dispersion as a function of latitude for Matuyama age data (0.78–2.58 Ma). Inset: Zoom-in of Jökuldalur results (this study and Udagawa et al. (1999)) and dispersion for a regional Iceland compilation (see Table S5-1, Suppl. Mat.). Mean dispersion from Jökuldalur (this study) shown as black. Mean dispersion from Jökuldalur (Udagawa et al., 1999) shown as orange. Mean dispersion from the Iceland compilation shown as purple. Mean dispersion from various global studies (Cromwell et al., 2013; Johnson et al., 2008; Lawrence et al., 2009; Opdyke et al., 2010; Panaiotu et al., 2012) shown in filled grey circles and regional compilations (cf. Johnson et al., 2008) in filled grey triangles. Errors bars are 2σ. All data have k > 50, and latitude cutoff of 45°. Blue line: Model G (McFadden et al., 1988). Green line: TK03 (Tauxe and Kent, 2004).

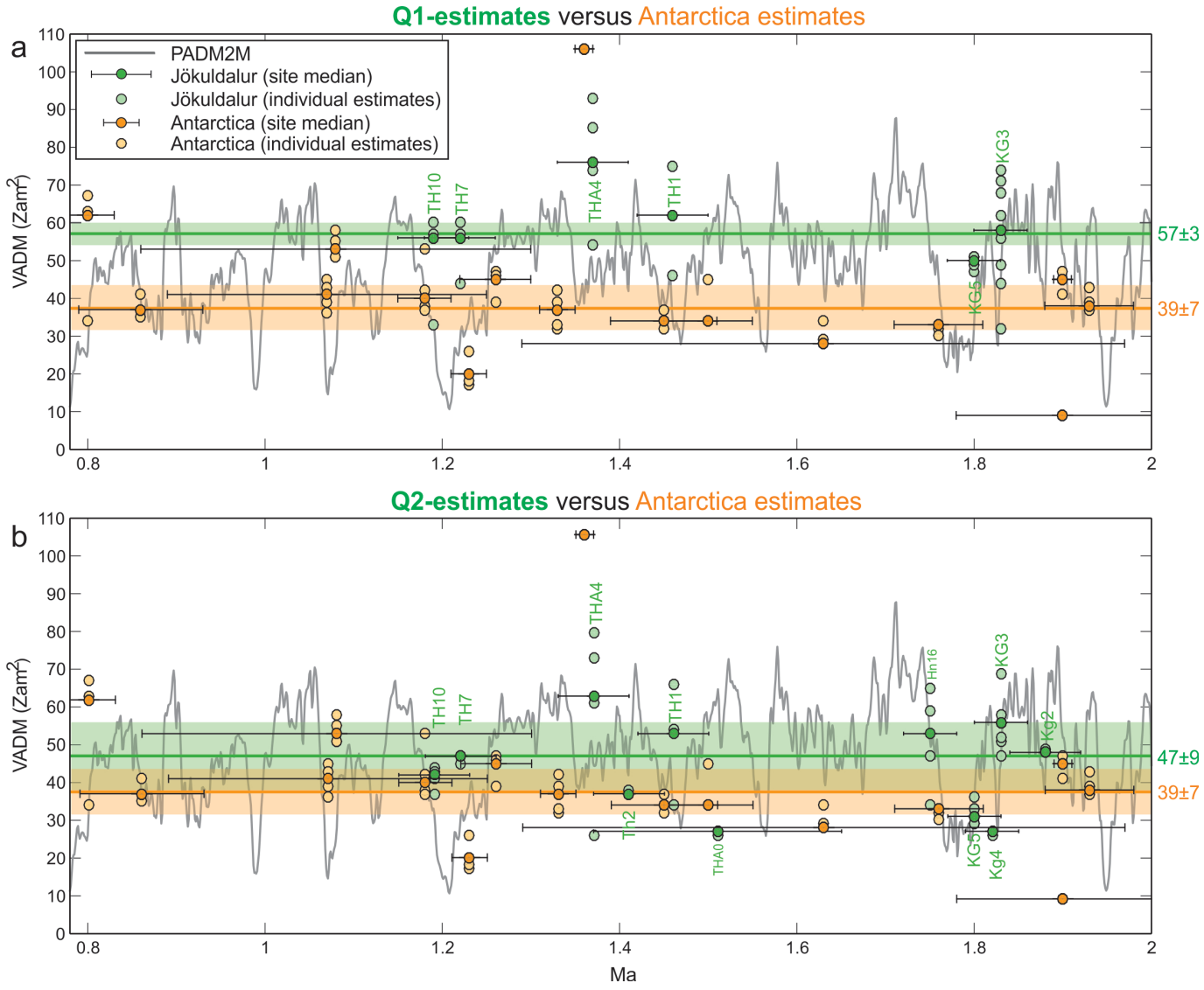


Figure 7: Virtual axial dipole moments (VADMs) versus time for the interval 0.78–2 Ma. Grey line: PADM2M time-varying paleomagnetic axial dipole moment model (Ziegler et al., 2011). Dark(light) filled green circles: Site-level median (dark) and individual (light) field strengths from Jökuldalur (this study). The ages of the Jökuldalur data are based on new Ar-Ar ages and from interpolated model ages (Section 6). All ages given with errorbars of 2σ. Dark(light) filled orange circles: 16 site-level median (dark) and individual (light) field strengths from Antarctica (Lawrence et al., 2009) that satisfy a site-level cut-off of N ≥3. (a) Preferred field strength estimates (Q1) from Jökuldalur (see Table 2). (b) Alternative field estimates (Q2) from Jökuldalur using the less strict specimen-level criteria of Lawrence et al. (2009) and a site-level cut-off of N ≥3 (see Table S4-2, Suppl. Mat.). We note that a higher median field is observed for the high-northern Q1 and Q2 data (green horizontal lines) as compared to the high-southern data (orange horizontal line). The horizontal lines are plotted with transparent horizontal bars according to their median absolute deviation.

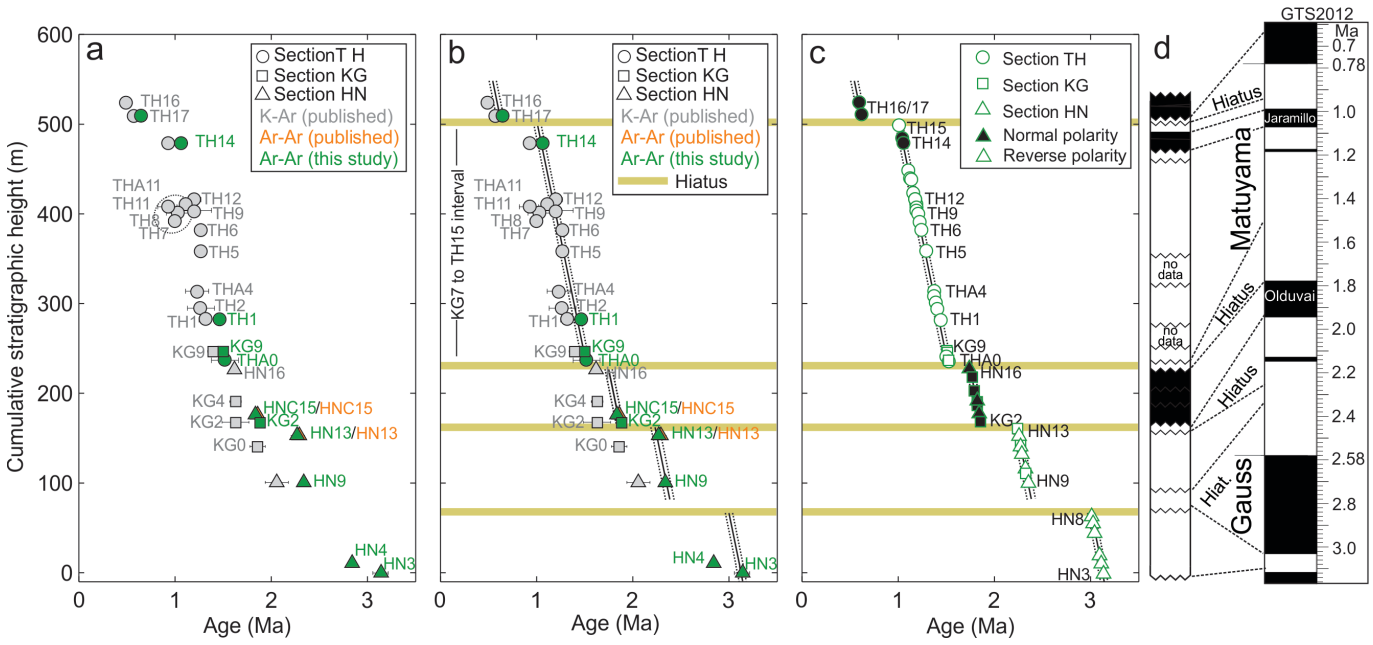


Figure 8: (a) K-Ar and Ar-Ar ages versus cumulative stratigraphic height (CSH) for sections TH, KG and HN in Jökuldalur. Published radiometric K-Ar and Ar-Ar ages are taken from Watkins et al. (1975), Udagawa et al. (1999) and Wijbrans and Langereis (2003), respectively. Only published ages from sites that can we confidently correlate to our sites are shown (cf. Table S6-1, Suppl. Mat.). New Ar-Ar ages are from this study. (b) 1^{st} order segmented regression model based on Ar-Ar data only. The regression model (thin black lines) is shown with 2σ error (thin dotted lines). Also shown are major hiati in the stratigraphic column. (c) Interpolated (model) ages for all sites according to their CSH. Black(white) symbols are normal(reverse) polarity. d) Revised magneto-chronostratigraphic model for sections TH, KG and HN based on correlation to GTS2012 (Gradstein et al., 2012). We find no evidence for the Gilsá event in sections KG or HN, where both normal polarity intervals can be correlated to the Olduvai subchron. We do, however, suggest that the short Jaramillo subchron is present near the top of section TH.